Applied Ocean Research 162 (2025) 104703

Contents lists available at ScienceDirect

Applied Ocean Research

journal homepage: www.elsevier.com/locate/apor

Research paper

Numerical investigation and experimental validation of INO WINDMOOR semi-submersible FOWT in extreme waves

Ahmet Soydan [a,*], Vilde Malmei [a], Petter Andreas Berthelsen [b], Widar W. Wang [a], Hans Bihs [a]

[a] Norwegian University of Science and Technology, Høgskoleringen 7A, 7491 Trondheim, Norway
[b] SINTEF Ocean, Trondheim, Norway

ARTICLE INFO

Keywords:
6DOF
Level set method
Immersed boundary
Direct forcing method
Mooring dynamics
MoorDyn
Fluid–structure interaction
REEF3D

ABSTRACT

Floating offshore wind turbines (FOWTs) are complex systems, as several physical phenomena are involved, and a complete numerical framework is essential for modeling such floating structures. In this study, the open-source hydrodynamics framework REEF3D is used to simulate the six-degrees-of-freedom (6DOF) motions of a moored floating body and a floating offshore wind turbine within a three-dimensional numerical wave tank (NWT). The numerical framework incorporates a quasi-static algorithm for mooring dynamics. A dynamic mooring model, MoorDyn, is also coupled with the FSI algorithm to assess the accuracy and reliability of the mooring algorithm. The mooring line tensions obtained by these models are compared against each other, and the motion responses of floating bodies are validated with the experimental results to demonstrate the accuracy of the numerical model. This study is also subjected to simulate dynamic responses of a floating wind turbine in highly nonlinear waves as well as very steep focused waves. To increase computational efficiency, Hydrodynamic-Coupling (HDC) between the fully nonlinear potential flow (FNPF) solver and the CFD solver in the open-source hydrodynamics framework is used to simulate the FOWT in focused waves. The numerical findings show that the HDC method increases computational efficiency without compromising accuracy.

1. Introduction

Floating offshore wind turbines (FOWTs) have gained significant attention as renewable energy technologies. FOWTs can exploit wind energy in deep water environments and the mooring systems play a critical role in ensuring safety and operational integrity in harsh marine conditions. Various numerical studies have been conducted in regular and extreme wave conditions to shed light on the reliability and efficiency of the different methods for FOWT simulations, including mooring effects.

1.1. Mooring modeling for FOWT

Wang et al. (2010) introduced a 3D quasi-static mooring model considering currents, soil resistance and cable elasticity, and Palm et al. (2017) presented a high-order discontinuous Galerkin method to capture snap loads in mooring lines. Mooring dynamics models have been coupled with the potential and Reynolds Averaged Navier–Stokes (RANS) equations-based solvers to estimate floating platform motions in waves. Masciola et al. (2011) coupled the floating wind turbine simulator FAST and OrcaFlex and evaluated the significance of mooring dynamics on the motion responses of FOWT (Masciola et al., 2013b). The numerical findings showed that the mooring line dynamics have small effects on the surge and heave motions. However, the mooring models have a significant influence on mooring line tensions. The quasi-static mooring model may underpredict the mooring forces in both regular and extreme wave conditions. Hall et al. (2011, 2014) also investigated the importance of mooring models for FOWT simulation by coupling FAST and a FEM-based dynamic mooring line model ProteusDS. The results indicate that the quasi-static mooring model can calculate the platform motion responses in regular waves; however, the error increased in extreme waves and the quasi-static mooring model could not capture the snap loads. Hall and Goupee (2015) validated a coupled model of FAST and a lumped-mass mooring model MoorDyn of the DeepCwind semi-submersible, showing that snap loads can be predicted by MoorDyn. Lozon and Hall (2023) enhanced OpenFAST model coupled with MoorDyn for shared-mooring floating offshore wind farms. Palm et al. (2016) coupled

* Corresponding author.
E-mail addresses: ahmet.soydan@ntnu.no (A. Soydan), vilde.malmei@hotmail.no (V. Malmei), petterandreas.berthelsen@sintef.no (P.A. Berthelsen), widar.w.wang@ntnu.no (W.W. Wang), hans.bihs@ntnu.no (H. Bihs).

https://doi.org/10.1016/j.apor.2025.104703
Received 10 April 2025; Received in revised form 16 June 2025; Accepted 14 July 2025
Available online 30 July 2025

OpenFOAM with MooDy and validated the method with a moored floating vertical cylinder. A moored box in regular waves was simulated by several researchers. Domínguez et al. (2019) used Smooth Particle Hydrodynamics code DualSPHysics coupled with MoorDyn, and Chen and Hall (2022) and Jeon et al. (2023) used OpenFOAM coupled with MoorDyn. The numerical results showed good agreement with the experimental data in motion responses, but some discrepancies were evident in mooring tensions. Chen et al. (2024) also developed a model in OpenFOAM coupled with MoorDyn to simulate multiple moored floating structures. The numerical results were compared with results of DualSPHysics solver and good agreements were shown.

1.2. CFD solvers coupled with mooring models for FOWT

Recently, semi-submersible floating offshore wind turbines (FOWTs) have been investigated in various scenarios to assess the reliability of computational fluid dynamics (CFD) codes. Validation of CFD codes coupled with mooring models has been a critical focus. Burmester et al. (2020) carried out a surge decay simulation of a FOWT with a catenary mooring line system to validate the open-source CFD code ReFRESCO (Vaz et al., 2009). Wang et al. (2021) employed a verification and validation (V&V) study using linear and dynamic mooring models in pitch free-decay motion. Significant improvements were obtained with the dynamic mooring model. Later, Wang et al. (2022a) coupled the dynamic mooring model MOORING3D (Huang and Chen, 2020) with ReFRESCO and performed a comprehensive V&V study under regular waves. Furthermore, Zhong et al. (2024) compared the performance of six different mooring line models for FOWTs. The results show that nonlinearity is introduced in the dynamic mooring model. In realistic scenarios, the FOWTs may encounter extreme wave conditions. Zhou et al. (2019) simulated a FOWT in focused waves using OpenFOAM with an in-house dynamic mooring model. Waves were generated by the open-source toolbox waves2Foam (Jacobsen et al., 2012) and the results were compared with the FAST code. A recent comparative study on the hydrodynamic response of a floating offshore wind turbine (FOWT) was presented by Yu et al. (2025). The study includes detailed numerical analyses for free decay tests and focused waves to assess the reliability of various tools, ranging from low-fidelity to high-fidelity.

1.3. Multi-physics coupled CFD solvers for FOWT

As an advancement of FOWT simulations, aerodynamic loads of the wind turbines were included in numerical applications. Liu et al. (2017) conducted a fully coupled CFD simulation with OpenFOAM, including aerodynamics, hydrodynamics, and mooring dynamics effects for the FOWT under various wave conditions. The rigid-body motion was handled with the overset mesh method, and a quasi-static mooring model calculated the mooring effects. The reciprocal interaction between the wind turbine and the FOWT was investigated by considering the wind speeds and wave conditions. Cheng et al. (2019) presented fully coupled aero-hydrodynamic numerical simulations with OpenFOAM. Aerodynamic analysis of a wind turbine was conducted with the unsteady actuator line model (UALM) (Li et al., 2015), and mooring dynamics was calculated with three catenary lines. The commercial CFD code STAR-CCM+ is also commonly used for fully coupled FOWT simulations. Tran and Kim (2016, 2018) carried out a multi-physical full-scale FOWT analysis for a free decay test under regular wave conditions. Platform motion was handled using an overset mesh, and mooring dynamics was solved with a quasi-static mooring model. Hydroelastic effects and structural flexibility have also become increasingly relevant for the design phase of FOTW platforms. Wei et al. (2024) presented a numerical framework with a quasi-static mooring solver integrated into a fully coupled CFD-discrete module beam (DMB) model for hydroelasticity simulations of very large floating structures (VLFS) in waves. The CFD solver OpenFOAM was coupled with the structure solver MBDyn, and the coupling scheme was validated with experimental data. The numerical findings indicated that hydroelastic behavior has a significant effect on the mooring system.

1.4. Coupled CFD-potential flow solvers

Concerning computational efficiency and accuracy, several studies have been conducted using the coupling of potential flow and CFD solvers for wave–structure interaction problems. Kim et al. (2010) integrated the boundary element method (BEM) with the volume of fluid (VOF) method for random wave propagation in a two-way coupling. The numerical results of the coupled model were almost identical to those of the single-VOF model, and the computational efficiency was improved. Gatin et al. (2017) presented a one-way coupling model in the foam-extend library using the High-Order Spectral (HOS) method and a CFD solver for realistic wave simulations. The numerical model was applied to several test cases, including a full-scale ship simulation under a 3D extreme wave, where the extreme wave was efficiently generated using the HOS method. Xu et al. (2021) also developed a coupled model in which the HOS method was used for wave propagation in the far-field region, while the wave-structure interaction in the near-field was calculated using the CFD solver Star-CCM+. The model was used to simulate floating production storage and offloading (FPSO) motions under irregular wave conditions. The numerical results demonstrated the potential of the coupling model for realistic wave-structure interaction simulations. Robaux and Benoit (2022) also developed a one-way coupling scheme using the fully nonlinear potential flow (FNPF) model and the RANS solver of OpenFOAM, and the method was validated using a fixed submerged body. It was shown that the computational time could be significantly reduced with the coupling method. Most recently, Zhang et al. (2023) coupled the HOS method with STAR-CCM+ to simulate a FOWT under 3-h irregular wave conditions and compared the results with OpenFAST. The numerical findings indicated that the proposed method improved the accuracy of the motion responses of the FOWT in comparison to OpenFAST and required fewer core hours for the simulations. Furthermore, Soydan et al. (2025) introduced an improved direct forcing immersed boundary method (DF-IBM) as an alternative tool for floating body simulations in waves. The numerical framework also enables Hydrodynamic-Coupling (HDC) between the fully non-linear potential flow (FNPF) solver and the CFD solver. As previously demonstrated by Wang et al. (2022b) and Kamath et al. (2022), wave propagation can be efficiently generated by the FNPF method, while the wave-structure interactions are calculated using the CFD solver in the near-field. This feature provides a suitable numerical scheme for the effective and accurate simulation of FOWTs in long-duration wave conditions.

1.5. Objectives of this paper

This study presents applications of the numerical framework introduced by Soydan et al. (2025). The improved DF-IBM offers a complete numerical framework tailored for simulating FOWTs in realistic ocean waves. The numerical model incorporates a quasi-static mooring model (Martin et al., 2021b), and the open-source lumped-mass mooring model MoorDyn (Hall and Goupee, 2015) is also coupled to the numerical framework to assess the significance of the fidelity of the mooring models. The method is applied to a FOWT in steep and extreme wave conditions to obtain new insights. For validation purposes, a 3D moored floating box is investigated in three different regular wave conditions to compare the quasi-static mooring model and MoorDyn. The motion responses and the mooring line tensions are shown with the experimental results. Subsequently, the method is applied to the triangular-shaped INO WINDMOOR semi-submersible FOWT design (Thys et al., 2021). WINDMOOR is a Competence Building Project (KPN) funded by the Research Council of Norway and offshore wind industry. This project aimed to enhance the understanding of the forces that govern the mooring system FOWTs (Silva de Souza et al., 2021). The FOWT was tested at a 1:40 Froude scale in the Ocean Basin at SINTEF Ocean, with three mooring lines used to restrain the platform's motion during the experiment. The FOWT is simulated in three distinct

wave conditions with increasing wave steepness using different mooring algorithms. The motion response results are presented alongside the experimental results and the importance of the mooring algorithms on the motion responses are discussed. The proposed method is also subjected to a test with very steep focused waves to demonstrate its robustness when large motion responses occur. A validation study is performed with a 2D floating body in a focused wave. Then the INO WINDMOOR semi-submersible FOWT is investigated under a very steep focused wave. Here, the Hydrodynamic-Coupling (HDC) feature of the numerical framework is used to reduce the computational resources. All numerical findings showcase the functionality and potential of the method.

2. Numerical model

The numerical framework REEF3D includes a fully non-linear potential flow model REEF3D::FNPF (Bihs et al., 2020) and a computational fluid dynamics (CFD) model REEF3D::CFD (Bihs et al., 2016). The FNPF solver is efficient in generating the waves and the CFD solver is capable of simulating wave-structure interaction and nonlinear waves. Details about these models are given in the following sections.

2.1. REEF3D::FNPF

The fully non-linear potential flow model REEF3D::FNPF solves the Laplace equation for the velocity potential ϕ, considering inviscid, incompressible and irrotational flow. The governing equation is written as:

$$\frac{\partial^2\phi}{\partial x^2}+\frac{\partial^2\phi}{\partial y^2}+\frac{\partial^2\phi}{\partial z^2}=0 \tag{1}$$

The Laplace equation can be solved with the kinematic and dynamic free surface boundary conditions and the kinematic bottom boundary condition. The kinematic free surface boundary condition indicates that the fluid particles always remain at the free surface η, formulated as in Eq. (2):

$$\frac{\partial\eta}{\partial t}=-\frac{\partial\eta}{\partial x}\frac{\partial\widetilde{\phi}}{\partial x}-\frac{\partial\eta}{\partial y}\frac{\partial\widetilde{\phi}}{\partial y}+\widetilde{w}\left(1+\left(\frac{\partial\eta}{\partial x}\right)^2+\left(\frac{\partial\eta}{\partial y}\right)^2\right), z=\eta \tag{2}$$

The dynamic free surface boundary condition enforces the pressure on the free surface to be equal to the atmospheric pressure as in Eq. (3):

$$\frac{\partial\widetilde{\phi}}{\partial t}=-\frac{1}{2}\left(\left(\frac{\partial\widetilde{\phi}}{\partial x}\right)^2+\left(\frac{\partial\widetilde{\phi}}{\partial y}\right)^2\right)+\frac{1}{2}\widetilde{w}^2\left(1+\left(\frac{\partial\eta}{\partial x}\right)^2+\left(\frac{\partial\eta}{\partial y}\right)^2\right)-g\eta, z=\eta \tag{3}$$

where $\widetilde{w}$ is the vertical velocity at the free surface. Finally, the kinematic bottom boundary condition satisfies that the fluid particle cannot penetrate the solid boundary as in Eq. (4).

$$\frac{\partial\phi}{\partial z}+\frac{\partial h}{\partial x}\frac{\partial\phi}{\partial x}+\frac{\partial h}{\partial y}\frac{\partial\phi}{\partial y}=0,\quad z=-h. \tag{4}$$

Here, $\widetilde{\phi}=\phi(\boldsymbol{x},\eta,t)$ represents the velocity potential with the horizontal location $\boldsymbol{x}=(x,y)$ at the free surface.

The Laplace equation is discretized with a second-order central differences scheme on a σ-coordinate grid and it is solved with the conjugated gradient BiCGStab algorithm of the hypre library (van der Vorst, 1992) with the geometric multigrid preconditioner PFMG (Ashby and Flagout, 1996). The σ-transformation is applied as in Eq. (5).

$$\sigma=\frac{z+h(\mathbf{x})}{\eta(\mathbf{x},t)+h(\mathbf{x})} \tag{5}$$

A fifth-order accurate weighted essentially non-oscillatory (WENO) scheme (Jiang and Shu, 1996) is applied for the spatial discretization of the free surface elevation and velocity potential. A third-order Total Variation Diminishing (TVD) Runge–Kutta scheme (Shu and Osher, 1988) is applied to solve the time derivatives. The time step size is controlled under the restriction of the CFL condition depending on the phase velocity. The method is fully parallelized based on the domain decomposition method and MPI library.

2.2. REEF3D::CFD

The continuity and Navier–Stokes (N–S) equations in convective form are solved in the 3D numerical wave tank (NWT) to satisfy the conservation of mass and momentum as follows:

$$\nabla\cdot\mathbf{u}=0 \tag{6}$$

$$\frac{\partial\mathbf{u}}{\partial t}+\mathbf{u}\cdot\nabla\mathbf{u}=-\frac{1}{\rho}\nabla p+\nu\nabla\cdot\left(\left[\nabla\mathbf{u}+\nabla\mathbf{u}^T\right]\right)+\mathbf{g} \tag{7}$$

where $\mathbf{u}$ is the velocity vector, ρ is the density of the fluid, p is the pressure, ν is the kinematic viscosity, and $\mathbf{g}$ the acceleration vector due to gravity. The k-ω turbulence model with an additional turbulent damping scheme at the free surface is used as a turbulence closure for the Reynolds-averaged Navier–Stokes equations (RANS), as referenced in Bihs et al. (2016).

The interface between the air and water phases is captured by the level set function (Osher and Sethian, 1988), which is defined as a signed distance function $\phi(\vec{x},t)$:

$$\phi(\vec{x},t)=\begin{cases}>0 & \text{if } \vec{x}\in\text{phase 1}\\ =0 & \text{if } \vec{x}\in\Gamma\\ <0 & \text{if } \vec{x}\in\text{phase 2}\end{cases} \tag{8}$$

The convection of the level set function is solved using the fluid velocity field $\mathbf{u}$.

$$\frac{\partial\phi}{\partial t}+\mathbf{u}\cdot\nabla\phi=0 \tag{9}$$

After transporting the free surface each time step, the level set function is initialized with a PDE-based reinitialization equation (Sussman et al., 1994) as in Eq. (10) to maintain the signed distance properties, $|\nabla\boldsymbol{\Phi}|=1$.

$$\frac{\partial\phi}{\partial t}+\mathrm{S}(\phi)\left(|\nabla\phi|-1\right)=0 \tag{10}$$

Here, $\mathrm{S}(\phi)$ is the smoothed sign function (Peng et al., 1999). Negative distance values ($\mathrm{S}(\phi)<0$) represent the air phase, positive values represent the water phase ($\mathrm{S}(\phi)<0$) and the zero value ($\mathrm{S}(\phi)=0$) indicates the interface between the air and water phases. The density and viscosity are defined for the whole domain using:

$$\rho=\rho_w H(\phi)+\rho_a(1-H(\phi)) \tag{11}$$

$$\nu=\nu_w H(\phi)+\nu_a(1-H(\phi)) \tag{12}$$

with the subscripts w and a indicating water and air properties, respectively. The smoothed Heaviside function $H(\phi)$ is then used for smoothing the sharp change of the fluid properties at the interface

$$H(\phi)=\begin{cases}0 & \text{if } \phi<-\epsilon\\ \frac{1}{2}\left(1+\frac{\phi}{\epsilon}+\frac{1}{\pi}\sin\left(\frac{\pi\phi}{\epsilon}\right)\right) & \text{if } |\phi|\le\epsilon\\ 1 & \text{if } \phi>\epsilon\end{cases} \tag{13}$$

with an interface thickness of $\epsilon=2.1\Delta x$ (Bihs et al., 2016).

The system of equations is solved using finite differences on a staggered rectilinear grid. A fifth-order accurate weighted essentially non-oscillatory (WENO) scheme (Jiang and Shu, 1996) is applied for the convection terms. The fifth-order accurate Hamilton–Jacobi WENO method of Jiang and Peng (2000) is used for discretization of the convection term in Eq. (9). For the diffusion terms, the second-order accurate central finite differences is applied. An incremental pressure-correction algorithm (Timmermans et al., 1996) is used for the solution

of the pressure gradient term in the RANS equation as described in Martin et al. (2021a). In the predictor step, the conservation equation for momentum Eq. (7) is solved without considering the pressure gradients. An intermediate velocity field $\mathbf{u}^{(*)}$ is calculated by an explicit third-order low-storage Runge–Kutta scheme (Spalart et al., 1991) using the following equation:

$$\frac{\mathbf{u}^{(*)}-\mathbf{u}^{(k-1)}}{\Delta t}=2\alpha_k\nu\nabla\cdot\left(\left[\nabla\mathbf{u}+\nabla\mathbf{u}^T\right]\right)^{(k-1)}-2\alpha_k\nabla\left(\frac{p^{k-1}}{\rho}\right)-\gamma_k\mathbf{u}^{k-1}\cdot\nabla\mathbf{u}^{k-1}-\zeta_k\mathbf{u}^{k-2}\cdot\nabla\mathbf{u}^{k-2}+\mathbf{g} \tag{14}$$

Here, α_k =4/15, 1/15, 1/6, γ_k =8/15, 5/12, 3/4, ζ_k = 0, −17/60, −5/12 and k = 1, 2, 3. The third-order Total Variation Diminishing (TVD) Runge–Kutta scheme (Shu and Osher, 1988) is applied for the solution of the time derivatives for Eqs. (9) and (10). The time step size is controlled under the restriction of the CFL condition to ensure numerical stability efficiently. An implicit Euler method is applied for the time advancement of k and ω equations to prevent a significantly smaller time step size due to the CFL criterion (Bihs et al., 2016). The diffusion term of the RANS equation is treated implicitly to remove it from the CFL restriction. The Poisson equation for the pressure correction is formed by the insertion of the intermediate velocities into the continuity equation.

$$\nabla\cdot\left(\frac{1}{\rho}\nabla p_{corr}\right)=\frac{1}{2\alpha_k\Delta t}\nabla\cdot\mathbf{u}^{(*)} \tag{15}$$

The Poisson equation is solved for the pressure correction terms p_{corr} with the fully parallelized BiCGStab algorithm of the hypre library (van der Vorst, 1992) with the geometric multigrid preconditioner PFMG (Ashby and Flagout, 1996) to increase the computational performance. Finally, the pressure and the divergence-free velocity field are calculated using the updated pressure correction term:

$$p^{(k+1)}=p^{(k)}+p_{corr} \tag{16}$$

$$\mathbf{u}^{(k+1)}=\mathbf{u}^{*}-\frac{2\alpha_k\Delta t}{\rho}\nabla p^{(k+1)} \tag{17}$$

2.2.1. FSI algorithm

In the numerical framework of REEF3D, the fluid–structure interaction algorithm is built upon a direct forcing immersed boundary method (DF-IBM). The governing equations are modified by adding a forcing term $\mathbf{f}$ in the momentum equations to take into account the rigid body velocity field in the Eulerian domain.

$$\nabla\cdot\mathbf{u}=0 \tag{18}$$

$$\frac{\partial\mathbf{u}}{\partial t}+\mathbf{u}\cdot\nabla\mathbf{u}=-\frac{1}{\rho}\nabla p+\mathbf{g}+\mathbf{f} \tag{19}$$

The forcing term $\mathbf{f}^{(*)}$ is calculated as in Eq. (20) and it is smeared out through the interface by using a smoothed Heaviside function.

$$\mathbf{f}^{(n+1)}\approx\mathbf{f}^{(*)}=H\left(\Phi_s^{(*)}\right)\cdot\left(\frac{\mathbf{P}(\mathbf{u}^{(*)})-\mathbf{u}^{*}}{2\alpha_k\Delta t}\right) \tag{20}$$

Here, $\mathbf{P(u)}$ is the rigid body velocity field, $\mathbf{u}^*$ is the fluid velocity field, α_k is a Runge–Kutta coefficient and Δt is time-step.

The signed distance field Φ_s is constructed with the level set function and added in the smoothed Heaviside function for tracking the fluid-solid interface, which is the zero level set (Φ_s = 0). The signed distance field is created with the information provided by an STL geometry representing the rigid body consisting of multiple non-connected triangles. The closest distance from neighboring fluid cells to the solid boundary is determined by a ray-casting algorithm (Bihs et al., 2017). The signed distance function Φ_s is reinitialized with the PDE-based Eq. (10) by Sussman et al. (1994) to keep the solid boundary obtained from the ray casting sharp.

The intermediate rigid-body velocity field is defined as Eq. (21), where $\dot{\boldsymbol{x}}_i$ is the translational rigid-body velocity vector, $\boldsymbol{\omega}_i$ is the angular rigid-body velocity vector and $\boldsymbol{r}$ is the distance vector to the center of gravity of the rigid body.

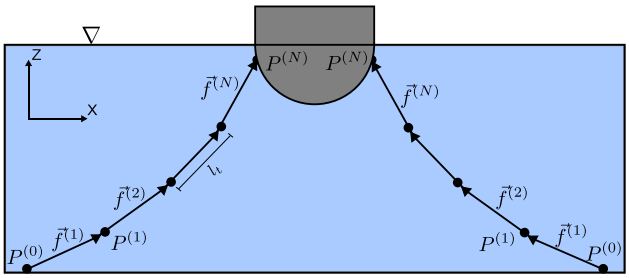

Fig. 1. Discrete mooring line — Quasi-static mooring model.

$$\mathbf{P}\left(\mathbf{u}^{(*)}\right)=\dot{\boldsymbol{x}}_i+\boldsymbol{\omega}_i\times\boldsymbol{r} \tag{21}$$

The body forces and momentum are obtained by integrating the fluid properties of pressure p, the viscous stress tensor τ over the discrete solid surface Ω:

$$\boldsymbol{F}_i=\int_{\Omega}(-\mathbf{n}p+\rho\nu\mathbf{n}\tau)d\Omega(\mathbf{x})=\sum_{i=1}^{N}(-\mathbf{n}p+\rho\nu\mathbf{n}\tau)_i\cdot\Delta\Omega_i \tag{22}$$

$$\boldsymbol{M}_i=\int_{\Omega}\mathbf{r}\times(-\mathbf{n}p+\rho\nu\mathbf{n}\tau)d\Omega(\mathbf{x})=\sum_{i=1}^{N}\mathbf{r}_i\times(-\mathbf{n}p+\rho\nu\mathbf{n}\tau)_i\cdot\Delta\Omega_i \tag{23}$$

where $\mathbf{n}$ is the surface normal vector on the solid body surface pointing outwards. The pressure p and the viscous stress tensor τ contributions of the solid surface area are integrated to calculate the global forces.

To accurately calculate the buoyancy and hydrodynamic forces, the grid resolution near the immersed boundary must be sufficiently fine. This is typically determined by a grid convergence study. For computational efficiency, local grid refinement can be applied in the vicinity of the body, rather than using a uniform fine mesh for the entire domain. This approach enables better resolution of the flow features around the immersed boundary without significantly increasing the total number of cells. Furthermore, to ensure proper interpolation between the Eulerian grid and the triangulated solid surface, the size of the triangles on the solid surface must be smaller than the local numerical grid size. If this criterion is not satisfied, the triangulated surface mesh is automatically refined during preprocessing to match the grid resolution. This ensures the accurate prediction of the forces and moments acting on the solid body. Further details on the implementation and applications of the DF-IBM can be found in Soydan et al. (2025) and Larkermani et al. (2025).

2.2.2. Quasi-static mooring dynamics model

A finite element-based quasistatic mooring model was implemented in the numerical framework REEF3D as presented in Martin et al. (2021b). The mooring forces are calculated as external forces and subsequently added to the total force during each Runge–Kutta substep. The mooring line dynamics, neglecting bending stiffness, are explained (Palm et al., 2017) as:

$$\gamma\frac{\partial^2\vec{r}}{\partial t^2}=\frac{\partial F_T\vec{f}}{\partial s}+\vec{F}_e \tag{24}$$

Here, γ represents the cable mass per unit length, F_T is the tension force magnitude, $\vec{f}$ is the unit vector in the same direction of the tension force, and $\vec{F}_e$ denotes the external forces, which include hydrodynamic and gravitation effects.

Eq. (24) is simplified, assuming that the flow is steady-state and the line motion is small in time:

$$\frac{\partial F_T\vec{f}}{\partial s}=-\vec{F}_e \tag{25}$$

As illustrated in Fig. 1, the mooring line is discretized with N bars. The bars have the same length of $\_\__l$ in two consecutive nodes P. The first node $P^{(0)}$ is connected to the bottom, and the last node $P^{(N)}$ is connected to the floating body. The gravity force contribution at each node $P^{(j)}$ is calculated using Eq. (26):

$$\vec{F}_G^j = \gamma \vec{g} \cdot \frac{\rho_m - \rho}{\rho_m} \cdot \frac{l_t^j + l_t^{j+1}}{2}, \quad j = 1, \ldots, N-1 \tag{26}$$

where ρ_m is the material density of the mooring line, and $\vec{g}$ is a unit vector pointing in the direction of the gravitational force. Hydrodynamic forces are calculated as drag forces using Morison's formula at each bar as in Eq. (27). The added mass forces are neglected in this model. Here, $\vec{v}$ is the velocity vector of the nodes considering the quiescent water, and c_n and c_t are the drag coefficients in normal and tangential directions, respectively. This formula contributes to the hydrodynamic mooring damping.

$$\begin{aligned}\vec{F}_H^j = l_t^j d_t^j \frac{\rho}{2} \cdot \Big[& c_t \left(\vec{v} \cdot \vec{f}\right) \|\vec{v} \cdot \vec{f}\| \cdot \vec{f} \\ & + c_n \left(\vec{v} - \left(\vec{v} \cdot \vec{f}\right) \vec{f}\right) \|\vec{v} - \left(\vec{v} \cdot \vec{f}\right) \vec{f}\| \Big], \quad j = 1, \ldots, N\end{aligned} \tag{27}$$

F_G depends on the bar length l_t according to Eq. (26), which is calculated as a polynomial of F_T. Here, K_p and k are the stiffness constants and iteration index, respectively.

$$l_{t,(k+1)}^j = \left[l_t^j \cdot \left\{ 1.0 + \sum_{p=1}^{P} K_p(j) \cdot \left(\frac{F_T^j + F_T^{j-1}}{2} \right)^p \right\} \right]_k, j = 1, \ldots, N \tag{28}$$

Then, the force equilibrium at each inner node can be found by separating the internal and external forces:

$$\vec{f}^{j+1} F_T^{j+1} - \vec{f}^{j} F_T^{j} = -\left(\vec{F}_H^j + \vec{F}_G^j\right), \quad j = 1, \ldots, N-1 \tag{29}$$

However, the mooring line has N bars and N–1 inner nodes, leading to an undetermined equation system. To solve this problem, the boundary condition is enforced by using the fixed end points of mooring line $P^{(0)}$ and $P^{(N)}$ as:

$$\sum_{j=1}^{N} \vec{f}^{j} l_t^j = \vec{x}\left(P^N\right) - \vec{x}\left(P^0\right) \tag{30}$$

Considering Eqs. (29) and (30), the linear system of equations is yielded, which is solved iteratively by Gaussian elimination method.

$$\begin{pmatrix} \mathbf{T} \\ \mathbf{L} \end{pmatrix} \cdot \mathbf{F} = \begin{pmatrix} -(\mathbf{H} + \mathbf{G}) \\ \vec{x}\left(P^N\right) - \vec{x}\left(P^0\right) \end{pmatrix} \tag{31}$$

Here, $\mathbf{T}$ is a sub-matrix of tension forces, $\mathbf{L}$ is the bar lengths vector, $\mathbf{H}$ and $\mathbf{G}$ are the sub-matrices of the hydrodynamic and static forces.

2.3. Lumped-mass mooring dynamics model

In this study, the lumped-mass mooring model MoorDyn (Hall and Goupee, 2015) is coupled with the numerical framework REEF3D. As depicted in Fig. 2, the mooring line is discretized into N equally distanced bars with N+1 nodes. The first and last nodes, $\mathbf{r}_0$ and $\mathbf{r}_N$, are connected to the bottom (anchor node) and the floating body (fairlead node). The line segment between two consecutive nodes has an index of $1/2$. Each node is represented by a global vector $\mathbf{r} = \mathbf{r}(x, y, z)$, defined in the inertial reference system. The tension in the segment of $i + 1/2$ is calculated as:

$$\mathbf{T}_{i+1/2} = E \frac{\pi}{4} d^2 \varepsilon_{i+1/2} \frac{\mathbf{r}_{i+1} - \mathbf{r}_i}{\|\mathbf{r}_{i+1} - \mathbf{r}_i\|} \tag{32}$$

where E is the Young's modulus, d is the diameter of the mooring line, $\varepsilon_{i+1/2} = \|\mathbf{r}_{i+1} - \mathbf{r}_i\| / l - 1$ is the strain, l is the unstretched length of the mooring line segment.

The hydrodynamic forces acting on the nodes in transverse direction $\mathbf{D}_{qi}$ and tangential direction $\mathbf{D}_{pi}$ are calculated based on Morison's equation.

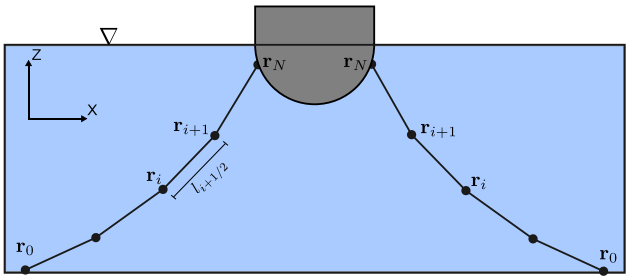

Fig. 2. Discrete mooring line — Lumped-mass mooring model.

The complete equation of motion for each node i obtained by considering the forces above with submerged weight $\mathbf{W}_i$ and the vertical force due to the mooring line seabed interaction $\mathbf{B}_i$ is:

$$\left[\mathbf{m}_i + \mathbf{a}_i\right] \ddot{r}_i = \mathbf{T}_{i+1/2} - \mathbf{T}_{i-1/2} + \mathbf{C}_{i+1/2} - \mathbf{C}_{i-1/2} + \mathbf{W}_i + \mathbf{B}_i + \mathbf{D}_{pi} + \mathbf{D}_{qi}, \tag{33}$$

where $\mathbf{C}_{i+1/2}$ is the internal damping force, $\mathbf{a}_i$ is the added mass and $\mathbf{m}_i = \frac{\pi}{4} d^2 l \rho \mathbf{I}$ is 3×3 mass matrix.

The system of equations above is solved for all nodes of the mooring line with a constant-time-step second-order Runge–Kutta (RK2) integration algorithm.

2.4. Coupling MoorDyn with FSI algorithm

This study aims to assess the accuracy and reliability of the quasi-static and dynamic mooring models. For this, the open-source lumped-mass mooring model MoorDyn (Hall and Goupee, 2015) is coupled with the numerical framework REEF3D. The flowchart of coupling between the rigid-body FSI algorithm of REEF3D and the lumped-mass mooring model MoorDyn (Hall and Goupee, 2015) can be seen in Fig. 3. The fluid solver is separated from the rigid-body dynamics solver, and communication is established through a two-way, non-iterative weak coupling method. Mooring forces and moments are also calculated independently and added to the total force acting on the floating body during each Runge–Kutta substep. The algorithm begins with the initialization of the fluid solver, rigid-body dynamics and MoorDyn. In the first iteration of the Runge–Kutta integration, the momentum predictor step (Eq. (19)) starts without the forcing term. Subsequently, the forces acting on the floating body are calculated, and the equations of motion are solved by the rigid-body dynamics solver to update the position and the velocity of the rigid body. The new position and velocity of the rigid body, along with the time step of the fluid solver, are transferred to MoorDyn. MoorDyn calculates the mooring dynamics and passes the summation of the mooring forces and moments to the rigid-body dynamics solver to be used in the next iteration of the Runge–Kutta integration. The rigid-body dynamics solver calculates the forcing term, which is added to the predicted momentum. Finally, the flow solver advances to the next iteration of the Runge–Kutta integration.

The time step, Δt, of the floating body dynamics and fluid solver is determined based on the CFL condition. This value is then communicated to MoorDyn at each time step. MoorDyn uses internal time step, Δt_M, and its time integration as follows:

- If $\Delta t < \Delta t_M$, then MoorDyn reduces its time step to match the flow solver by setting $\Delta t_M = \Delta t$
- If $\Delta t > \Delta t_M$, then MoorDyn performs multiple internal steps with Δt_M during one flow solver time step to reach Δt.

Therefore, this coupling approach imposes no constraints on the global time step. The time step is governed by the requirements of the fluid solver (CFL condition.)

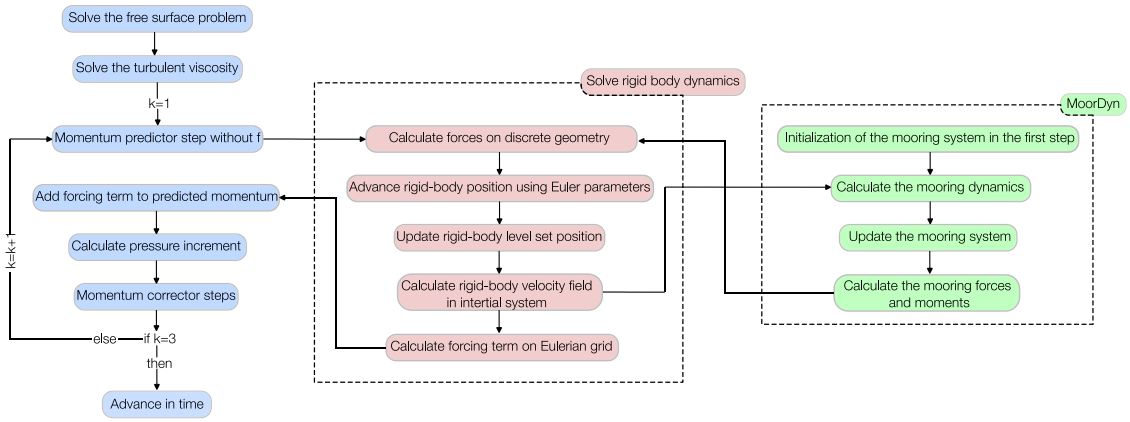

Fig. 3. Illustration of the 6DOF algorithm, k represents the Runge–Kutta substep iteration number.

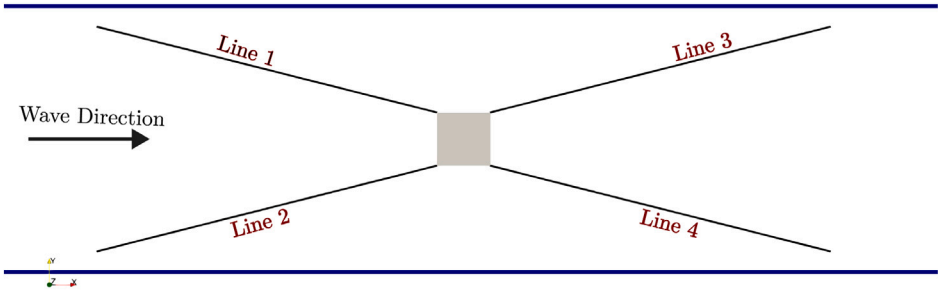

(a) Mooring lines of the floating box

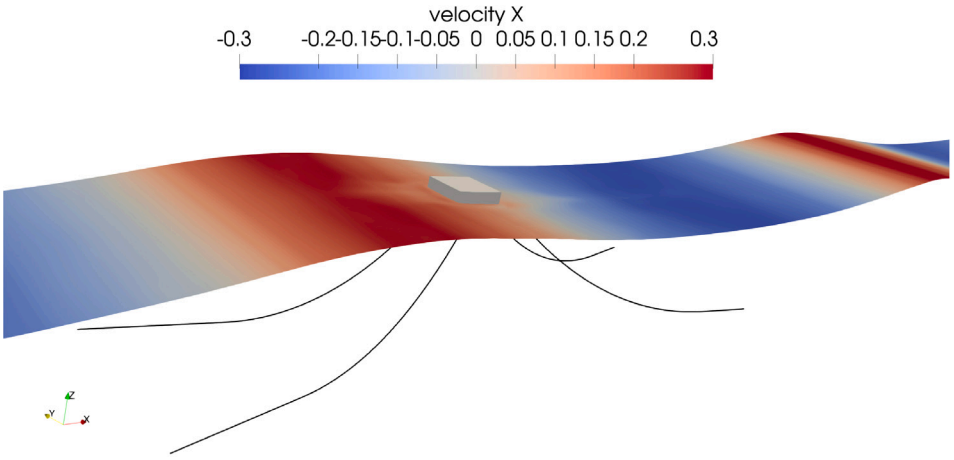

(b) Mooring lines of the floating box with the free surface

Fig. 4. Illustration of the mooring lines of the floating box.

3. Results

3.1. Moored floating box

A 3D moored floating cubic box under regular waves is addressed to compare the mooring algorithms. The experimental data is obtained from Wu et al. (2019), and the mooring setup is based on the work of Chen and Hall (2022) and Domínguez et al. (2019). The numerical framework incorporates wave generation and absorption methods (Miquel et al., 2018). Here, the relaxation method is used for both the wave generation and absorption zones. The wave generation and absorption zone lengths are one wavelength and two wavelengths, respectively. The numerical wave tank (NWT) dimensions are 10 m × 1 m × 1 m and the water depth d = 0.5 m between the wave generation and absorption zones. The box (0.2 m × 0.2 m × 0.132 m) is placed in the NWT at x = 3.5 m and the initial draft is 0.0786 m. The mass of the barge is 3.6 kg. The box moment of inertia I_{xx}, I_{yy}, I_{zz} is 0.015, 0.015 and 0.021 kg m^2. The box is simulated under three different regular wave conditions, as specified in Table 1. A 2nd-order Stokes theory is used to generate the waves.

The box motions are restrained with four mooring lines in waves as depicted in Fig. 4. The line diameter is 0.003656 m, the line mass

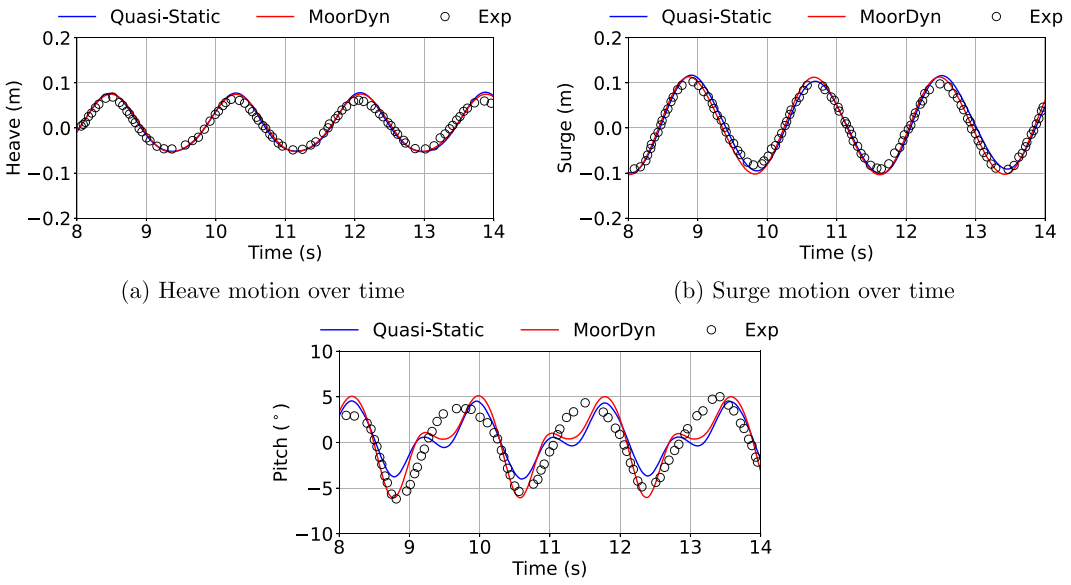

(a) Heave motion over time

(b) Surge motion over time

(c) Pitch motion over time

Fig. 5. 3DOF motion of the three-dimensional barge over time. Comparison of numerical and experimental results in Wave-1.

Table 1
Wave conditions for the moored floating box.

Wave conditions	Wave height H (m)	Wave period T (s)	Wave length L (m)
Wave - 1	0.12	1.8	3.57
Wave - 2	0.12	2.0	4.06
Wave - 3	0.15	1.8	3.57

per unit length is 0.0607 kg/m, the line length is 1.455 m and the axial stiffness is 19 N. More information about the mooring lines can be found in Chen and Hall (2022). For comparison, the motion responses of the box and corresponding mooring tensions are calculated with a quasi-static mooring model (Martin et al., 2021b) and the lumped-mass mooring model MoorDyn (Hall and Goupee, 2015). The mooring lines are divided into 40 elements. The same settings and parameters (mooring line diameter, mooring line mass per unit length, mooring line length, and mooring axial stiffness) are used for both mooring models. These two models calculate the mooring tensions, and the results are presented . The numerical error metrics of the motion responses obtained from both mooring models are quantified using the normalized mean absolute error (NMAE), as defined in Eq. (34) where n is the number of data points, y_{num} denotes the numerical values, and y_{exp} represents the experimental values. The numerical error metrics are presented in Table 2.

$$NMAE = \frac{1}{n}\sum_{i=1}^{n}\frac{\left|y_{exp,i} - y_{num,i}\right|}{\left|max(y_{exp}) - min(y_{exp})\right|} \tag{34}$$

According to the grid convergence study in Appendix A, $dx = 0.02$ m is selected for the numerical simulations. Figs. 5, 6, and 7 show the wave excitation motions of the floating box in three wave conditions: Wave-1, Wave-2, and Wave-3. Small differences can be observed in the heave motions obtained with both mooring models, but the results show good agreement in amplitude and phase. The surge motions in Wave-1 and Wave-2 are depicted in Figs. 5(b) and 6(b). The numerical results demonstrate good agreement despite slight over- and underestimations for peaks and troughs. Overall, both mooring models provide similar results. Larger differences are observed in the pitch motions. Earlier studies (Palm et al., 2016; Martin et al., 2021b) revealed that the pitch motion highly depends on the moment of inertia and center of mass of the floating body. The uncertainties in these parameters in the experiments may cause these differences in the pitch motion signals. Furthermore, Domínguez et al. (2019) remarked that a wood plate was used on the box's front face to measure the box motions in waves. The incoming waves splashed on this plate, and this additional geometry was not modeled in the numerical simulation. This could be the source of the discrepancy between the numerical and experimental results. The same discrepancy was also observed in the work carried out with OpenFOAM and MoorDyn (Chen and Hall, 2022), and in other work by Domínguez et al. (2019), where the DualSPHysics code and MoorDyn were used. The absence of the wood plate in the numerical simulation may be the reason for this, as explained in previous works (Chen and Hall, 2022; Domínguez et al., 2019). Nevertheless, the phase of the motion can be captured with both mooring models. The results obtained with MoorDyn can resolve the troughs of the pitch amplitudes better compared to the results obtained with the quasi-static mooring model.

Another possible source of discrepancy in the pitch motion is the occurrence of slacking events in the mooring lines. Fig. 8 presents the anchor tensions of Line-1 and Line-3 calculated by the quasi-static mooring model and MoorDyn. Neither mooring model can capture the slacking events observed in the experimental results, which may effect the accuracy of the pitch motion. For Wave-1 and Wave-2, both mooring models predict larger tensions in Line-1. The anchor tensions measured by Line-3 are quite acceptable, but MoorDyn can capture the low tensions better. Special attention is given to the anchor tensions for Wave-3, which is the steepest wave. Both mooring models underestimate line tensions in Line-1, similar to the results obtained with OpenFOAM and MoorDyn (Chen and Hall, 2022). On the other hand, the anchor tension in Line-3 shows good agreement with the experimental results for both mooring models. The most interesting result can be observed that the quasi-static mooring model exhibits a result similar to MoorDyn for Wave-3. Chen and Hall (2022) showed that the quasi-static mooring model, Mooring Analysis Program (MAP++) (Masciola et al., 2013a), coupled with OpenFOAM, underestimates the mooring line tensions in both Line-1 and Line-3. This may be because MAP++ does not take into account hydrodynamic forces. On the contrary, the quasi-static mooring model in the numerical framework REEF3D

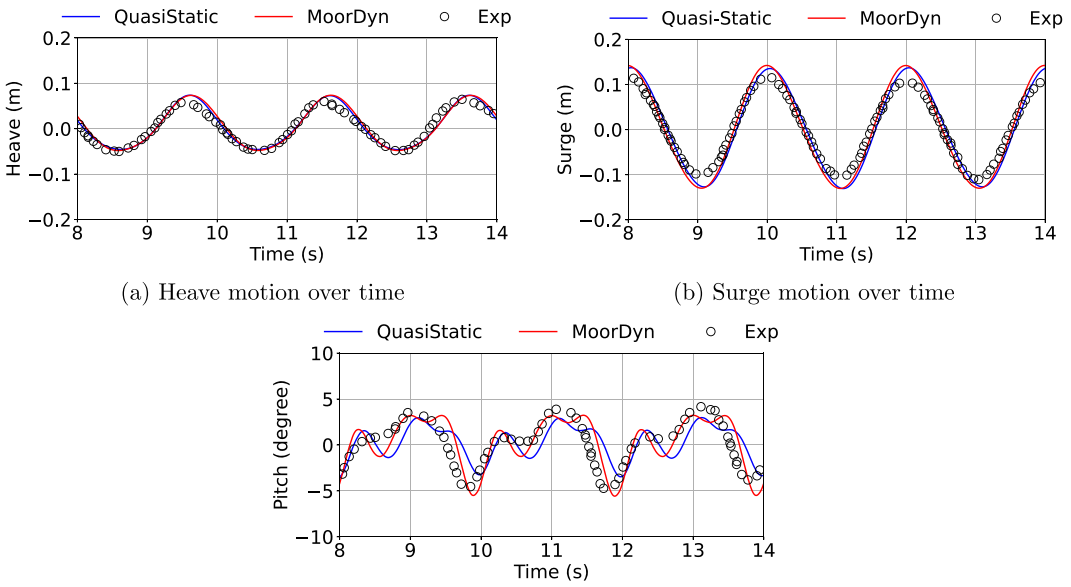

(a) Heave motion over time

(b) Surge motion over time

(c) Pitch motion over time

Fig. 6. 3DOF motion of the three-dimensional barge over time. Comparison of numerical and experimental results in Wave-2.

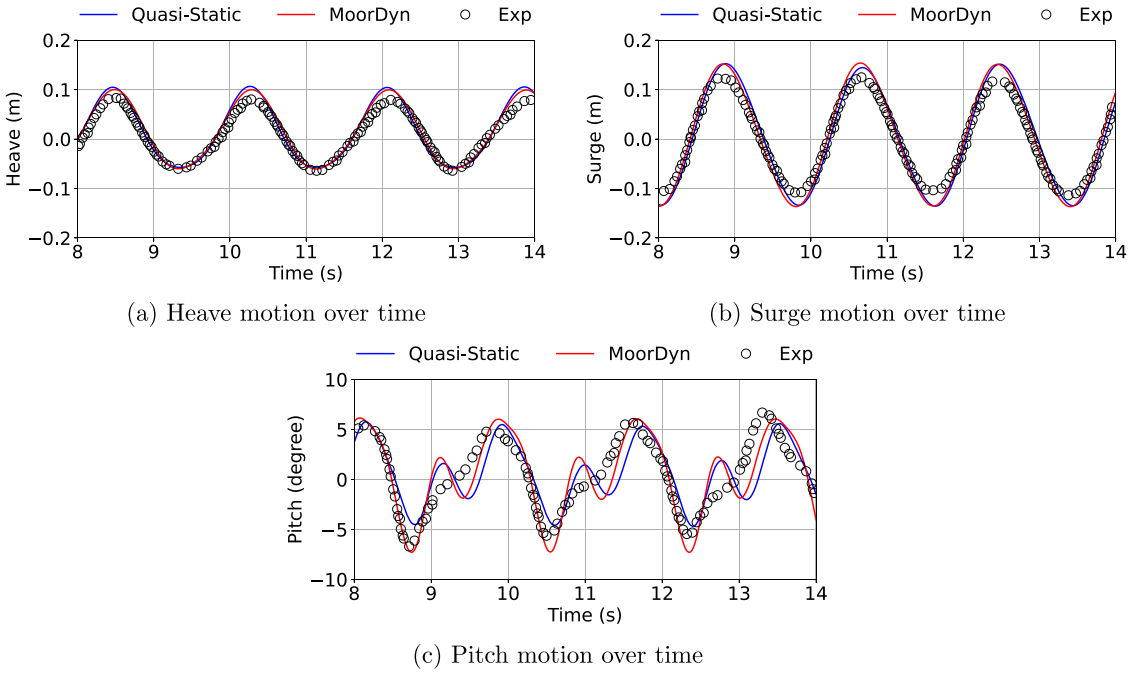

(a) Heave motion over time

(b) Surge motion over time

(c) Pitch motion over time

Fig. 7. 3DOF motion of the three-dimensional barge over time. Comparison of numerical and experimental results in Wave-3.

calculates the hydrodynamic forces based on Morrison's formula. The results presented here also indicate that the mooring line tensions have a minor effect on the floating body motion responses in regular wave conditions.

3.2. Windmoor semi-submersible floating offshore wind turbine

The improved rigid-body FSI algorithm is used to simulate the new prototype INO WINDMOOR semi-submersible wind turbine (Silva de Souza et al., 2021). The triangular-shaped floating structure has three vertical cylinders connected to deck beams and pontoons, as illustrated in Fig. 9. The main dimensions of the structure are given in Table 3. The experiment was carried out in SINTEF Ocean's Ocean Basin at a 1:40 Froude scale (Thys et al., 2021). The dimensions of the basin are 80 m × 50 m × 3.75 m (Berthelsen et al., 2022). The structure properties are outlined in Table 5.

Three mooring lines are used to restrain the motions of the semi-submersible in waves as depicted in Fig. 10. The coordinates of the mooring lines are given in Table 4. The mooring line tensions are obtained by the quasi-static mooring model and MoorDyn. The mooring line settings are the same for both models and the mooring lines are divided into 40 elements. It should be mentioned that the mooring lines

Table 2
The normalized mean absolute error for the motion responses of the moored floating box.

Motion	Wave - 1		Wave - 2		Wave - 3	
	Quasi-Static	MoorDyn	Quasi-Static	MoorDyn	Quasi-Static	MoorDyn
Heave	7.16%	6.71%	6.42%	7.86%	8.06%	7.42%
Surge	4.48%	4.42%	7.57%	7.98%	7.35%	7.35%
Pitch	14.60%	12.61%	17.31%	12.66%	13.28%	10.51%

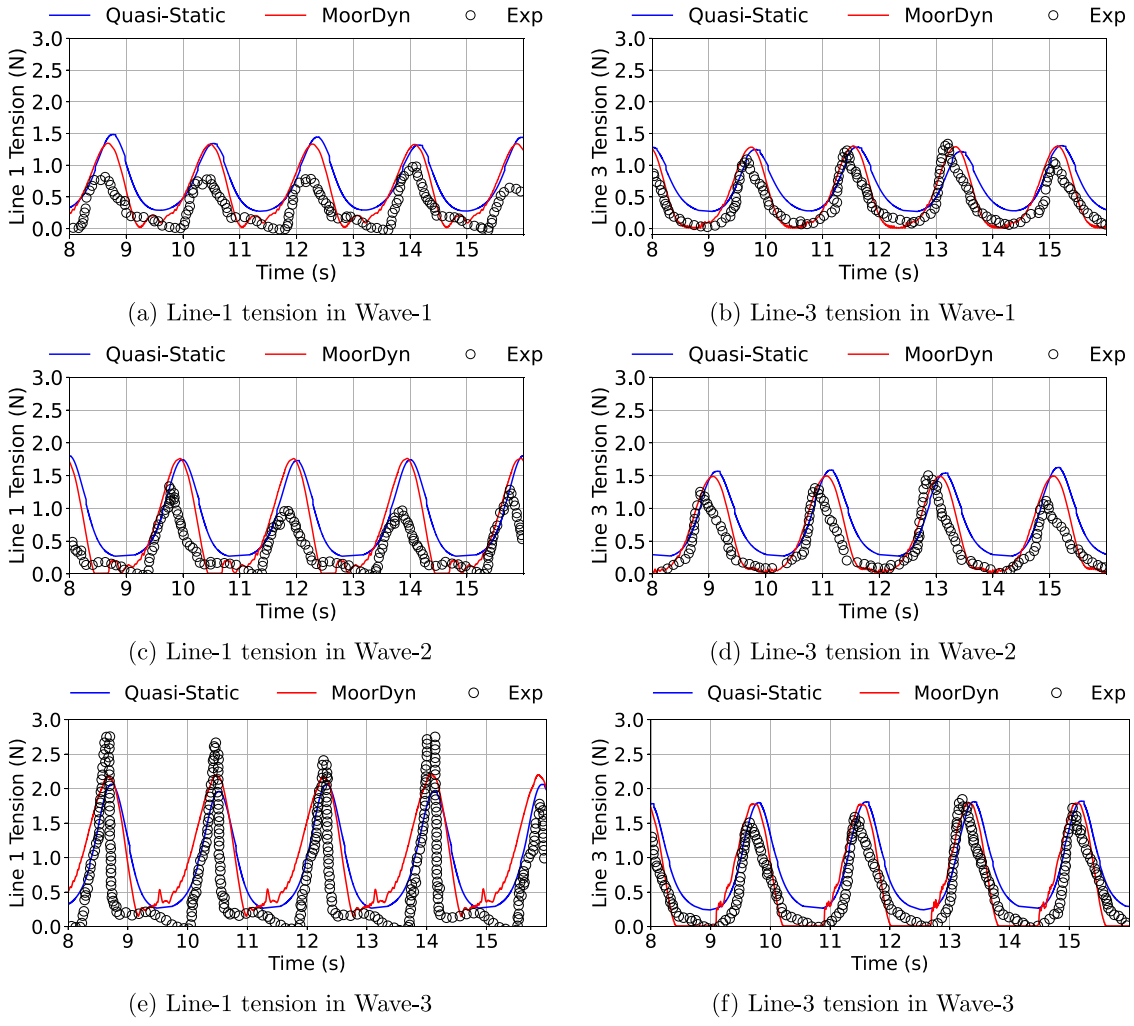

(a) Line-1 tension in Wave-1
(b) Line-3 tension in Wave-1
(c) Line-1 tension in Wave-2
(d) Line-3 tension in Wave-2
(e) Line-1 tension in Wave-3
(f) Line-3 tension in Wave-3

Fig. 8. Comparison of mooring line tensions of the floating box.

Table 3
Main dimensions of the INO WINDMOOR structure.

Column diameter	15.0 m
Column height	31.0 m
Pontoon width	10.0 m
Pontoon height	4.0 m
Column center-center distance	61.0 m
Deck-beam width	3.5 m
Deck-beam height	3.5 m
Draft	15.5 m

are above the water to exclude the hydrodynamic loads and mooring damping in the experiment.

3.2.1. Heave decay test

First, a heave decay test is performed. The simulation was carried out at model scale but the results are presented at full scale. The platform releases a position offset of 2.5 m (at full scale) from the equilibrium position. Three distinct grids are used for the simulation carried out in model scale: dx = 0.05 m, 0.025 m, and 0.01 m. The quasi-static mooring model is used in the heave decay test.

The time series of the heave decay motion for different grids is given in Fig. 11(a) and the corresponding power spectral density (PSD) of the heave decay motion is given in Fig. 11(b). The results converge monotonically as the grid sizes are refined. The coarse grid $dx = 0.05$ m shows a good match with the experimental results until 2.0 s however, the motion damping is too much after the first period of the motion. The fine grid dx = 0.01 m exhibits excellent agreement with the experimental results with a slight overshooting in the first peak of the motion. Fig. 11(b) also indicates that the fine grid can estimate the natural frequency of the heave motion with very good accuracy.

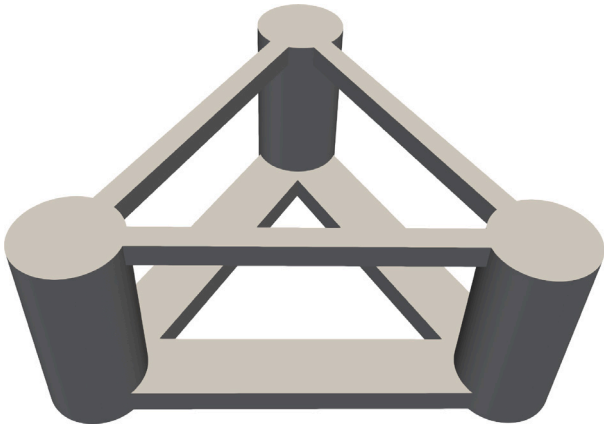

Fig. 9. INO WINDMOOR semi-submersible structure.

Table 4
Coordinates of mooring lines.

Line	Fairleads points (m)	Anchor points (m)
1	−21.759, 37.688, 15.500	−574.800, 967.280, 92.400
2	43.518, 0.000, 15.500	1345.690, 0.000, 99.200
3	−21.759, −37.688, 15.500	−582.475, −1000.200,100.000

Table 5
Windmoor system structural properties.

Mass	14 124.0 t
Draft	15.5 m
COG_z	3.95 m
r_{xx}	43.62 m
r_{yy}	44.01 m
r_{zz}	28.97 m
Natural periods	
Surge	93.8 s
Heave	16.6 s
Pitch	30.4 s

3.2.2. Regular wave

The semi-submersible structure is simulated under three distinct regular wave conditions as tabulated in Table 6. Wave-1 and Wave-2 are generated with a 2nd-order Stokes theory, while Wave-3 is generated with a 5th-order Stokes theory, which is the most nonlinear and the steepest waves. The relaxation method is employed for both wave generation and absorption zones. The aerodynamic loads are not considered in the presented study. All numerical errors based on NMAE (Eq. (34))are quantified in Table 7.

According to the grid convergence study in Appendix B, $dx = 0.025$ m is selected for the numerical simulations. Fig. 12 presents the motion responses of the semi-submersible in Wave-1, where the wave steepness is 1:120. Fig. 12(a) shows the heave motion responses. The results calculated with the two mooring models exhibit slight overestimation in peaks and troughs, yet demonstrate good agreement with the experimental results. PSD of the heave motion is given in Fig. 12(b). The largest motion is seen at the incident wave frequency. The surge motion responses and corresponding PSD are given in Fig. 12(c) and (d). The motion phase matches quite well, however small differences can be seen in the motion amplitudes obtained with the quasi-static mooring model. Besides showing the largest peak at the incident wave frequency, the PSD result of the surge motion also exhibits a second peak representing the surge natural frequency of the semi-submersible. 12(e) and (f) present pitch motion responses and pitch motion PSD in Wave-1. Irregularities are evident in the numerical results but this cannot be seen in the experimental result. Here, three distinct peaks in the PSD results obtained from the numerical calculations demonstrate the surge and pitch natural frequencies of the semi-submersible and incident wave frequencies. However, the second largest peak at the pitch natural frequencies cannot be observed in the experimental result. Overall, the numerical results show good agreement.

The wave excitation motions of the semi-submersible in Wave-2 are given in Fig. 13. The wave steepness here is 1:30. Fig. 13(a) shows the heave motion results. Excellent results are obtained with both mooring models. The surge and pitch results, on the other hand, exhibit small over- and undershooting in the peaks and troughs. Yet, the results are satisfactorily good. The largest peak is observed at the incident wave frequency in the PSDs of the motions in Fig. 13(b), (d) and (f) while a second peak frequency is evident at the pitch natural frequencies in pitch motion PSD (Fig. 13(f)).

The most challenging wave condition is Wave-3, which is the steepest wave, where the steepness is 1:15. Motion responses in Wave-3 are given in Fig. 14. The motions PSDs show a second peak at the first harmonic of that wave, as the wave is very steep. The numerical results show small differences, yet good agreement can be obtained. The experimental results exhibit a slow variation in the surge motion at a low frequency, which can also be observed in the numerical results. However, this variation is slightly more dominant in the numerical results. After all, the pitch motion amplitude obtained by the numerical calculations is quite similar to the experimental results. The irregular behavior is apparent in the experimental pitch motion. The numerical results slightly over- and underestimate the peaks and troughs but showcase generally good agreement.

In the numerical results for Wave-1 and Wave-2 conditions, a secondary peak at the system's natural pitch frequency (corresponding to a period of approximately 30.4 s) arises from the initial transient responses of the structure. This transient phase corresponds to the pitch natural frequency triggered by initial numerical perturbations before the system reaches a state of dynamic equilibrium. As the wave field fully develops, these transient motions are gradually damped out and the system reaches the wave-dominated motion. If the initial time series is trimmed from the pitch motion signal, the pitch motion PSD no longer shows this peak as shown in Fig. 15 for the pitch excitation motion in Wave-1. This effect is observed in Wave-1 and Wave-2 conditions, which involve lower wave excitation, allowing transient motion to be more pronounced. In contrast, under the higher excitation of Wave-3, the system rapidly reaches wave-dominated motion, and no such secondary peak is present.

Fig. 16 shows the FOWT free-surface interaction with vertical velocity contour. The wave diffraction and radiation occur due to wave–structure interaction in Wave-1 (Fig. 16(a) and (b)) and Wave-2 (Fig. 16(c) and (d)). The steepest wave, Wave-3, leads to large motions and strong nonlinear wave-structure interaction is evident (Fig. 16(e) and (f)).

Figs. 17–19 present the mooring line tensions calculated by the quasi-static mooring model and MoorDyn. Here, the hydrodynamic damping of the mooring lines is zero since the mooring lines are above the water. The peak and mean values of the Line-1 and Line-3 tensions are similar for both mooring models. Line-2 tension calculated with the quasi-static mooring model is a bit larger than MoorDyn results. The difference in the mean tension of Line-2 (aligned with the wave direction) between the quasi-static model and MoorDyn might arise from the dynamic response of the FOWT. Since Line-2 is directly aligned with the wave direction, it experiences significant dynamic loads due to platform surge motion. This is also evident in the amplitude of the mooring tension in Line-2. The quasi-static mooring model neglects added mass and line acceleration, whereas MoorDyn includes these effects, along with internal damping. As wave excitation is more dominant in this direction, the dynamic mooring model MoorDyn predicts different values.

The largest peak is seen at the incident wave frequency in the PSDs of the mooring line tensions. The peaks corresponding to the

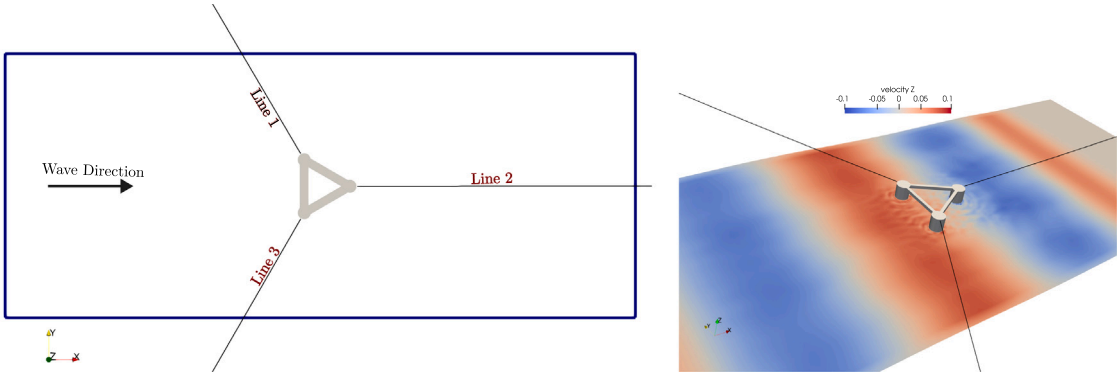

(a) Mooring lines of the Windmoor FOWT (b) Mooring lines of the Windmoor FOWT with free-surface

Fig. 10. Illustration of the mooring lines of the Windmoor FOWT.

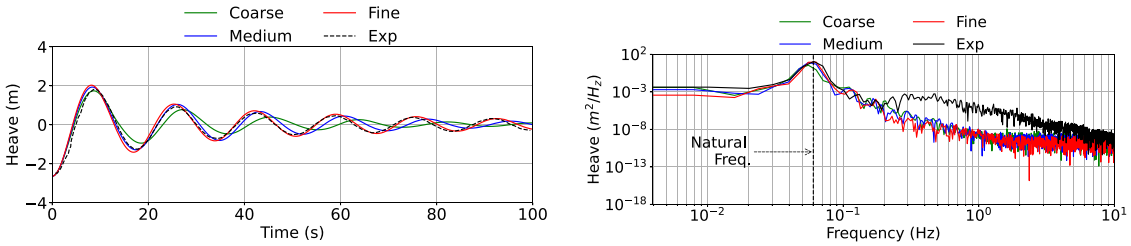

(a) Comparison of the heave motion over time (b) Comparison of the heave motion PSDs

Fig. 11. Grid convergence study for the heave decay test of the Windmoor FOWT.

Table 6
Wave conditions for the Windmoor FOWT.

Scale ratio 1:40	Model scale		Full scale	
Wave conditions	Wave height H (m)	Wave period T (s)	Wave height H (m)	Wave period T (s)
Wave - 1	0.06375	2.213594	2.55	14.0
Wave - 2	0.15750	1.739252	6.30	11.0
Wave - 3	0.31475	1.739252	12.59	11.0

Table 7
The normalized mean absolute error for the motion responses of the Windmoor FOWT.

Motion	Wave - 1		Wave - 2		Wave - 3	
	Quasi-Static	MoorDyn	Quasi-Static	MoorDyn	Quasi-Static	MoorDyn
Heave	5.45%	5.45%	3.05%	3.09%	5.05%	6.79%
Surge	6.47%	5.51%	4.77%	6.39%	8.95%	12.66%
Pitch	11.04%	7.77%	5.71%	5.74%	14.60%	14.14%

surge, pitch and heave natural frequencies of the semi-submersible are obtained with both mooring models in Wave-1 in Fig. 17(b), (d) and (f). The quasi-static mooring model can capture the excitations at the higher frequencies in Line-1 and Line-3 but the quasi-static mooring model cannot capture the peak at 0.12 Hz. In Wave-2, there is a peak at around 0.14 Hz for Line-1 and Line-3, and a peak at 0.12 Hz for Line-2 calculated by MoorDyn, which is not seen in the results obtained by the quasi-static mooring model. Similarly, the peak at 0.15 Hz in Line-1 and Line-3 and the peak at 0.105 Hz in Line-2 in Wave-3 are not calculated with the quasi-static mooring model. Given the mooring lines of the semi-submersible are above the water and hydrodynamic damping is not a subject considered in this study, these differences may stem from the assumption of steady-state flow and small line motion in time in the quasi-static mooring model. Nevertheless, the effect of the mooring line algorithm has small effects on the motion responses in regular wave conditions.

3.3. Free floating box in focused wave

FOWTs can also encounter extreme wave events when operating in deep water, where heavy wave loads act on the offshore structure, leading to large wave excitation motions and nonlinear wave-structure interactions. It is crucial to accurately simulate large motions while maintaining numerical stability. This section focuses on the floating body-focused wave interaction. First, the numerical method is validated with a 2D floating body simulation under a wave packet. The same numerical study was carried out by Hadžić et al. (2005), Barreiro et al. (2016) and Bouscasse et al. (2013). The experimental results are taken

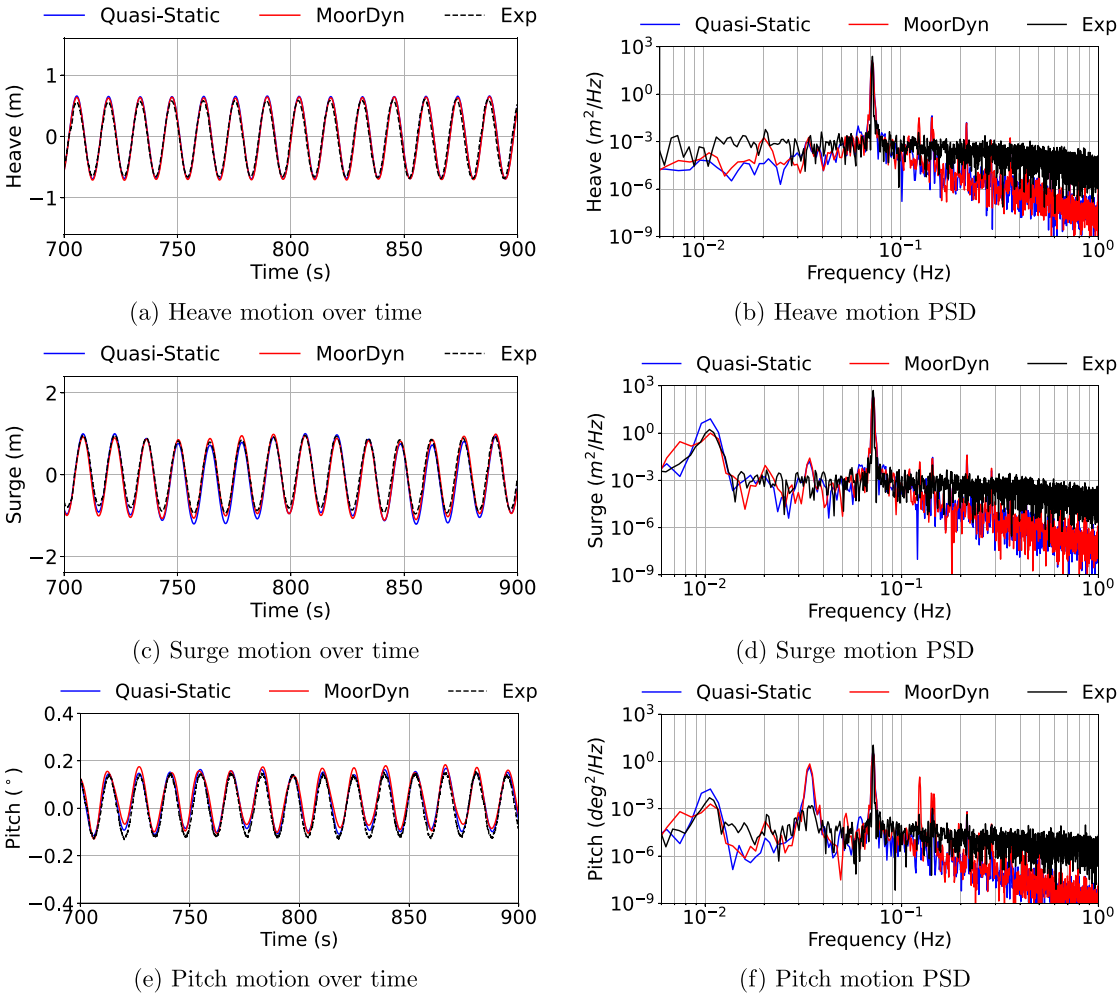

(a) Heave motion over time (b) Heave motion PSD

(c) Surge motion over time (d) Surge motion PSD

(e) Pitch motion over time (f) Pitch motion PSD

Fig. 12. Wave excitation motion of the Windmoor FOWT and corresponding PSDs. Comparison of numerical and experimental results in Wave-1.

from Hadžić et al. (2005). The floating body is a rectangular box with a length of 0.1 m, a height of 0.05 m and a density of 680 kg/m^3. The numerical domain is 8.0 m long, the water depth is 0.4 m and the floating body is placed at $x = 2.11$ m. The wave packet is generated with a flap wavemaker, whose time history of the angle is given in Fig. 21. The focusing point of the wave packet is at the center of the floating body. The wave is absorbed in the numerical beach at the end of the domain, which has a length of 1.5 m. The numerical setup is depicted in Fig. 20. Wave elevations were recorded by two probes placed at $x = 1.16$ m and $x = 2.66$ m.

According to the grid convergence study in Appendix C, $dx = 0.010$ is selected for the numerical simulations. The experimental and numerical time series of the motion responses are given in Fig. 23. The numerical result of the fine grid is presented here, demonstrating very good agreement. Additionally, Fig. 22 depicts the free-surface deformations and the positions of the floating body at $t = 7.2$ s and $t = 7.59$ s. The results exhibit a good match with the experiments.

3.4. Windmoor in focused wave with HDC

After validating the interaction between focused waves and a floating body in the previous section, the INO Windmoor semi-submersible is investigated under very steep focused waves. In the open-source hydrodynamics framework, Hydrodynamic Coupling (HDC) between the fully nonlinear potential flow (FNPF) solver and the CFD solver is available, as described by Wang et al. (2022b) and Kamath et al. (2022). This coupling scheme allows for the generation of long-duration waves using the FNPF method, while wave-structure interactions are calculated in a smaller domain to improve computational efficiency. Here, the simulation of the semi-submersible is carried out at the model scale and the results are also presented at the model scale. First, a validation study is carried out in 2D NWT for the focused wave generation with FNPF and HDC. The NWT of FNPF domain is 200 m long and the water depth is $d = 4.01$ m. The wave is generated with the FNPF model at the inlet boundary with the Dirichlet boundary condition and the wave is absorbed with the active wave absorption method. The CFD domain is 30 m long starting at 110 m, where the hydrodynamic coupling is applied and ends at 140 m. The FNPF solution is used as a wave boundary condition for the CFD solver in a one-way coupling as depicted in Fig. 24. The wave is initialized in the coupling zone following the relaxation method. A uniform horizontal grid size is $dx = 0.1$ m and 10 cells are used in the vertical direction for the FNPF model. The selected numerical grid for CFD calculations in regular waves is used for HDC-CFD calculations. The validation case for the focused wave generation is taken from Bihs et al. (2019). The wave packet method is applied to generate the focused waves. The significant wave height of the focused wave is $H_s = 1.18$ m. this is equivalent to 47.2 m in full scale. The significant wave period is $T_s = 7.39$ s. The focused point is $X_f = 126.21$ and the focused time is $T_f = 103$ s. The wave frequency band is between 0.2 rad/s and 3.5 rad/s. The number of wave components $N = 500$ for the wave generation. The FNPF model propagates the waves for 200 s and the CFD model obtains the wave

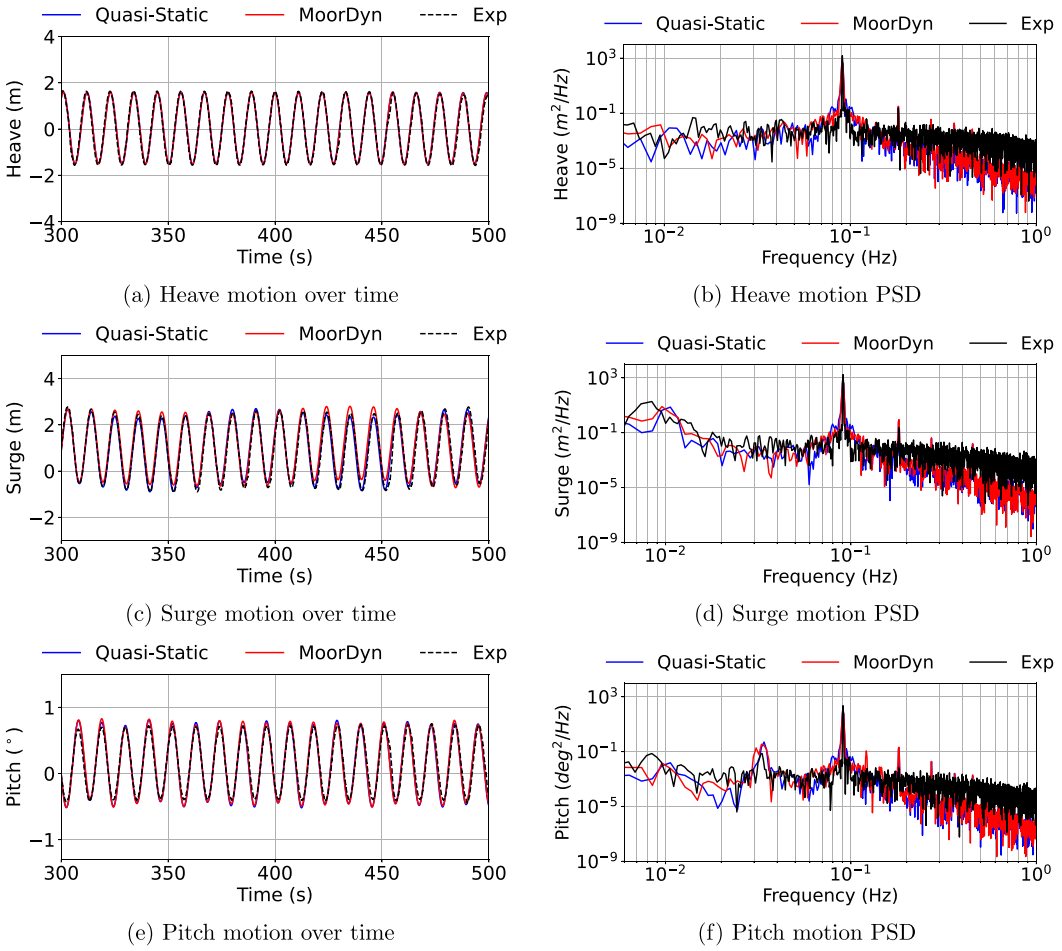

(a) Heave motion over time

(b) Heave motion PSD

(c) Surge motion over time

(d) Surge motion PSD

(e) Pitch motion over time

(f) Pitch motion PSD

Fig. 13. Wave excitation motion of the Windmoor FOWT and corresponding PSDs. Comparison of numerical and experimental results in Wave-2.

information in space and time from 93 s from the FNPF model. Then the CFD model simulates the waves for 30 s including the focused time $T_f = 103$ s. The time history of the wave elevation at the focused point $X_f = 126.21$ obtained from the FNPF, CFD and HDC model are compared with the experimental results in Fig. 25. The results are shifted in time considering the focusing time. The models can precisely capture the peak of the focused wave, while the HDC method shows a slightly larger secondary wave before the focusing point. In general, the HDC method can generate focused waves with a small difference.

Then the 3D numerical simulation is carried out for the semi-submersible focused wave interaction. The semi-submersible is placed at the focused point $X_f = 126.21$. The heave and surge motion of the semi-submersible and the mooring line tensions are shown in Fig. 26. The results obtained with both mooring models are similar. Fig. 27 shows the free surface structure interaction.

This numerical study showcases all the functionality of the numerical framework for FOWT simulations. Mooring lines can be modeled with the quasi-static mooring model or MoorDyn. The improved method can maintain numerical stability when dealing with large motion responses in extreme wave conditions, and highly nonlinear interaction is captured with the CFD solver, as shown in Fig. 27. With the HDC scheme, the length of the CFD domain is greatly reduced and only the results in the desired time interval are calculated. Thus, the computational cost of the CFD is substantially decreased. The CFD calculations in the desired time interval for the semi-submersible are carried out on a M1 Max Macbook Pro, 30 s of simulation takes ca. 6 h using 8 processors.

4. Conclusion

In this study, the applications of the improved DF-IBM for the FOWT semi-submersible in extreme waves are presented. The numerical model incorporates a native quasi-static mooring model to restrain the motion of the floating body in waves. The lumped-mass mooring model, MoorDyn, was also implemented in the numerical framework to assess the reliability of the mooring algorithm.

A 3D moored floating cubic box was simulated under the three distinct regular wave conditions to compare the quasi-static mooring model and MoorDyn. Both mooring models produced similar results, while MoorDyn can capture better the mooring line tensions. Both mooring models cannot model slacking events observed in experimental results, which might effect the accuracy of the pitch motion. Future enhancements will also include wave-induced loads on mooring lines to improve the prediction of the mooring line tensions. Overall, the mooring line tensions have a small effect on the motion responses of the floating body in regular waves.

The improved DF-IBM was used to simulate the INO WINDMOOR semi-submersible wind turbine in regular waves. First, a heave decay test was conducted to evaluate how accurately the buoyancy and added mass force could be calculated with the numerical framework. A grid convergence study was employed with the quasi-static mooring model, showing monotonic convergence. The heave natural frequency of the semi-submersible was calculated precisely with the fine mesh. Then the semi-submersible was simulated in three regular wave conditions by increasing the wave steepness. The results were obtained by using

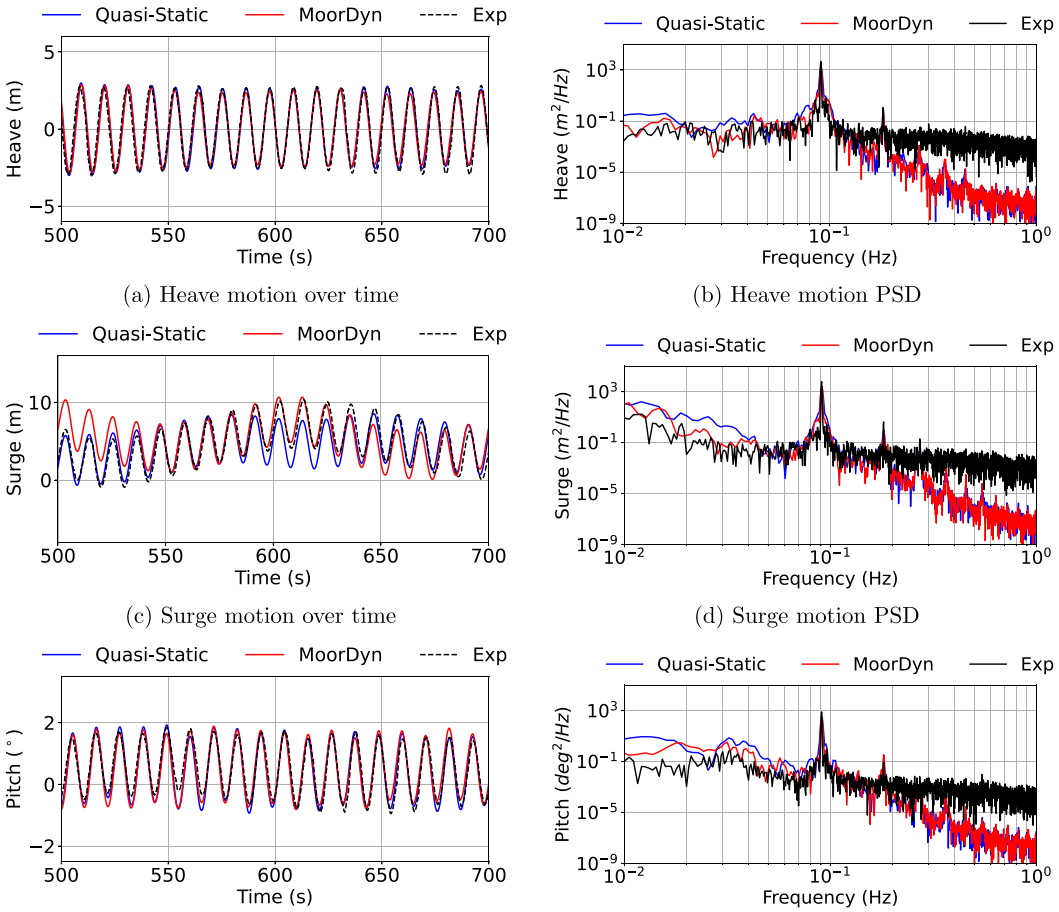

(a) Heave motion over time (b) Heave motion PSD

(c) Surge motion over time (d) Surge motion PSD

(e) Pitch motion over time (f) Pitch motion PSD

Fig. 14. Wave excitation motion of the Windmoor FOWT and corresponding PSDs. Comparison of numerical and experimental results in Wave-3.

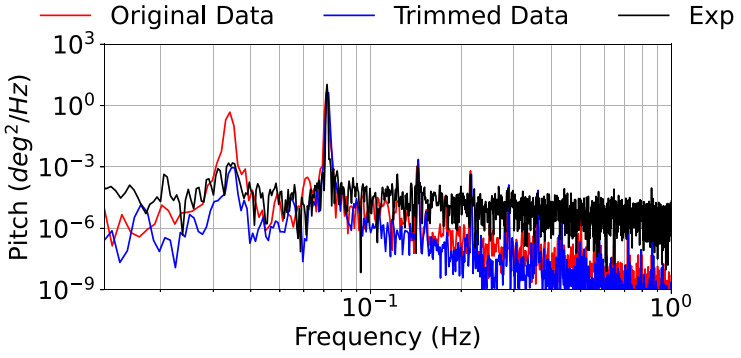

Fig. 15. PSD of the pitch excitation motion in Wave-1. The red line represents the original data. The blue one is the trimmed data.

the quasi-static mooring model and MoorDyn. Good agreement was observed between the numerical and experimental results. The improved method was able to handle to the most challenging, Wave-3, leading to large motion responses and highly nonlinear wave-floating body interaction. It was also observed that the quasi-static mooring model was not able to capture some peaks in the line tension PSDs, yet no significant effect was observed on the motion responses.

The numerical framework was also tested under very steep focused waves. Initially, a validation study was conducted using a 2D floating body. A very steep wave packet was generated with a flap wavemaker, resulting in nonlinear behaviors in both the free surface and the motion responses, accurately captured by the numerical method. Then the semi-submersible was investigated under a very steep focused wave. The HDC method was used for this case to increase the computational efficiency. The FNPF model generated the wave propagation in the NWT, and the wave information in time and space was transferred to the HDC zone in a one-way coupling to simulate wave-structure interaction with CFD. The peak of the focused wave can be captured precisely, although discrepancies are observed before and after the focusing point. As future work, the focused wave will be generated

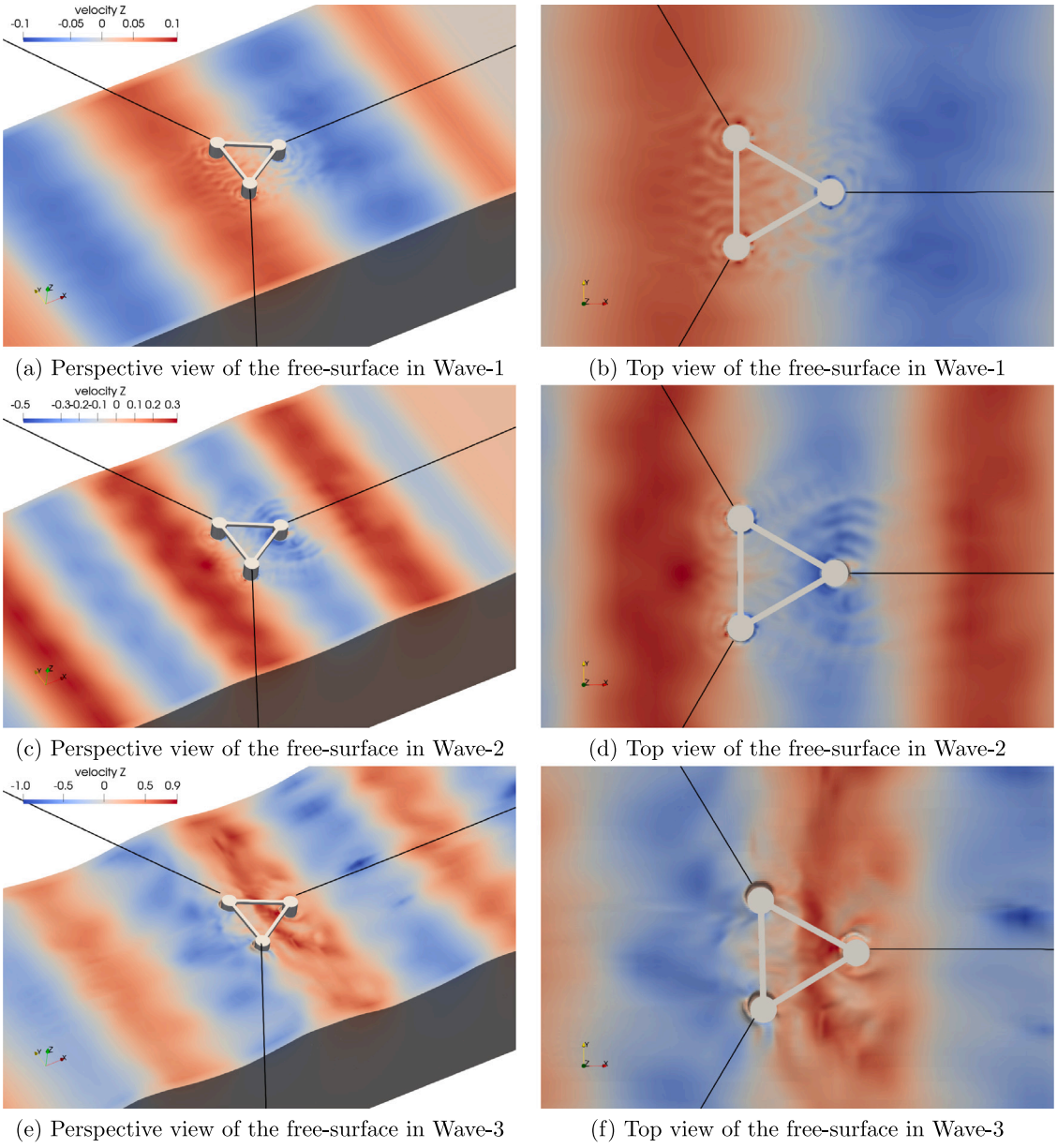

(a) Perspective view of the free-surface in Wave-1 (b) Top view of the free-surface in Wave-1

(c) Perspective view of the free-surface in Wave-2 (d) Top view of the free-surface in Wave-2

(e) Perspective view of the free-surface in Wave-3 (f) Top view of the free-surface in Wave-3

Fig. 16. The FOWT free-surface interactions, showing the vertical velocity contour.

using an actual flap wave maker to better replicate wave propagation in the NWT. Nevertheless, the numerical results revealed that the HDC method increases computational efficiency and can model the hydrodynamic interaction of floating bodies in extreme waves.

In conclusion, the method presented in this study offers a complete numerical framework including FNPF and CFD solvers, and mooring dynamic algorithm for wave-floating structure interaction problems.

CRediT authorship contribution statement

Ahmet Soydan: Writing – original draft, Visualization, Validation, Software, Conceptualization. **Vilde Malmei:** Validation, Investigation. **Petter Andreas Berthelsen:** Writing – review & editing, Supervision, Resources. **Widar W. Wang:** Writing – review & editing, Supervision. **Hans Bihs:** Writing – review & editing, Supervision, Software, Conceptualization.

Declaration of competing interest

The authors declare that they have no known competing financial interests or personal relationships that could have appeared to influence the work reported in this paper.

Acknowledgments

This work was made possible through the knowledge-building project Improving Performance in Real Sea, IPIRiS, financially supported by the Norwegian Research Council, NFR project number 308843, and the consortium partners.

The authors are also grateful to the WINDMOOR project, funded by the Research Council of Norway under the ENERGIX programme (grant no. 294573) for access to experimental data of the INO WINDMOOR floating substructure.

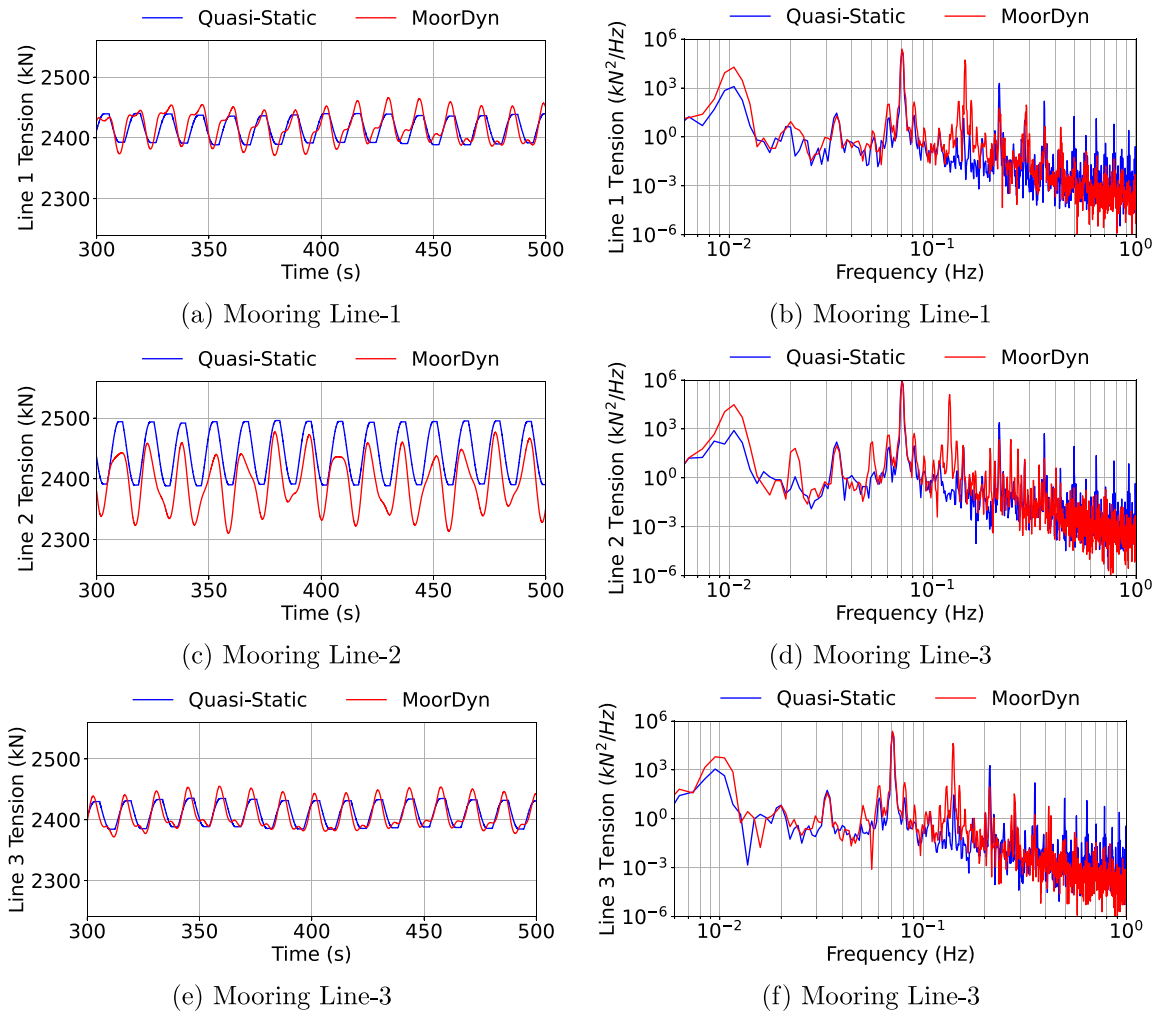

(a) Mooring Line-1 (b) Mooring Line-1

(c) Mooring Line-2 (d) Mooring Line-3

(e) Mooring Line-3 (f) Mooring Line-3

Fig. 17. Comparison of fairlead tensions and corresponding PSDs in Wave-1.

Appendix A. Grid convergence study for the moored floating box

A grid convergence study is carried out for Wave-1 with three uniform grids: $dx = 0.08$ m, 0.04 m, and 0.02 m. The quasi-static mooring model is used in the grid convergence study. The CFL number 0.1 is used throughout the all numerical studies. Time series for heave, pitch, surge motions, and the wave elevation at $x = 4.05$ m are given in Fig. A.28, together with the experimental results. The results converge as the grid size is refined. The results with the coarse grid show an offset in the heave motion. The numerical results exhibit good agreement with the experimental results for the heave, surge motions, and wave elevation with the medium and fine mesh. The maximum deviation between the numerical and experimental results is less than 8%. However, some discrepancy arises in the pitch motion. As a result, the fine grid is selected for the comparison of the mooring algorithms as it can capture the amplitude and phase very well.

Appendix B. Grid convergence study for Windmoor semi-submersible floating offshore wind turbine

A grid convergence study is employed for the semi-submersible in Wave-1. The minimum grid size is set as $dx = 0.1$ m, 0.05 m, 0.025 m and 0.015 m by using grid stretching with a stretching ratio of 1.1 as illustrated in Fig. B.29. The maximum grid size in the stretching area is applied as five times the minimum grid size. The quasi-static mooring model is used in the grid convergence study. The numerical results are presented in Fig. B.30 with the experimental results. In the heave motion responses in Fig. B.30(a), the coarse grid $dx = 0.1$ m shows somewhat overestimation in the peaks and the troughs. The results with fine grid $dx = 0.025$ m and finest grid $dx = 0.015$ m are quite similar. The surge motion results are presented in Fig. B.30(b). The best results are obtained with the fine grid $dx = 0.025$ m and finest grid $dx = 0.015$ m. The pitch motion (Fig. B.30(a)) is very sensitive to the grid resolution. The coarse grid $dx = 0.1$ m cannot capture the motion. It is noteworthy that the pitch motion amplitudes are quite small which is about 0.1° so that makes it very difficult to be captured precisely. Nevertheless, the fine grid $dx = 0.025$ m and the finest grid $dx = 0.015$ m provide acceptable results and the fine grid $dx = 0.025$ m is selected for the other simulations for the sake of computational efficiency and accuracy. The maximum deviation between the numerical and experimental results is less than 11%.

Appendix C. Grid convergence study for free floating box in focused wave

A grid convergence study is employed with three uniform grids: $dx = 0.016, 0.010, 0.0067$. The CFL number is set to 0.3. The time series of the wave elevations are given in Fig. C.31(a) and (b) along with

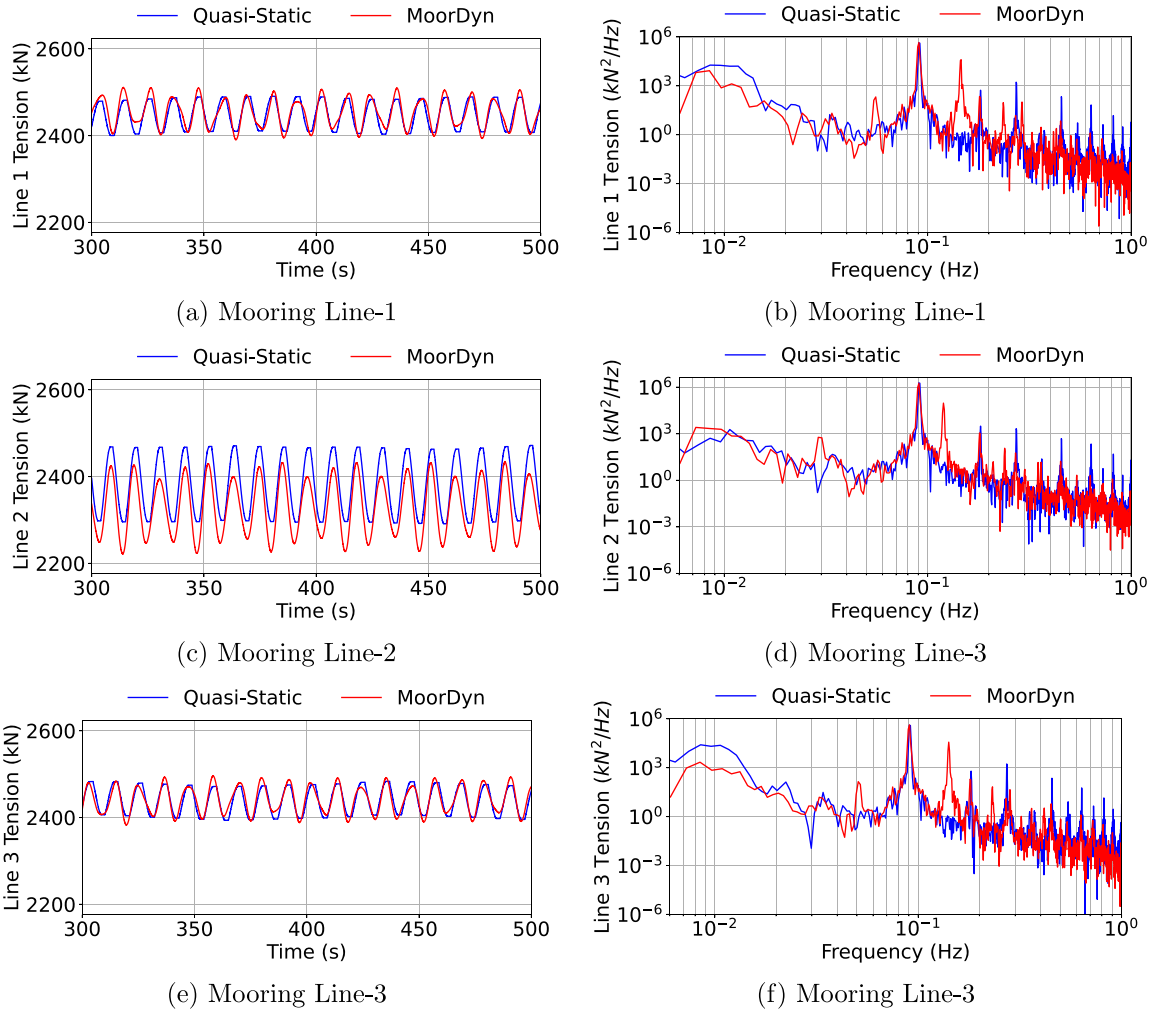

(a) Mooring Line-1 (b) Mooring Line-1

(c) Mooring Line-2 (d) Mooring Line-3

(e) Mooring Line-3 (f) Mooring Line-3

Fig. 18. Comparison of fairlead tensions and corresponding PSDs in Wave-2.

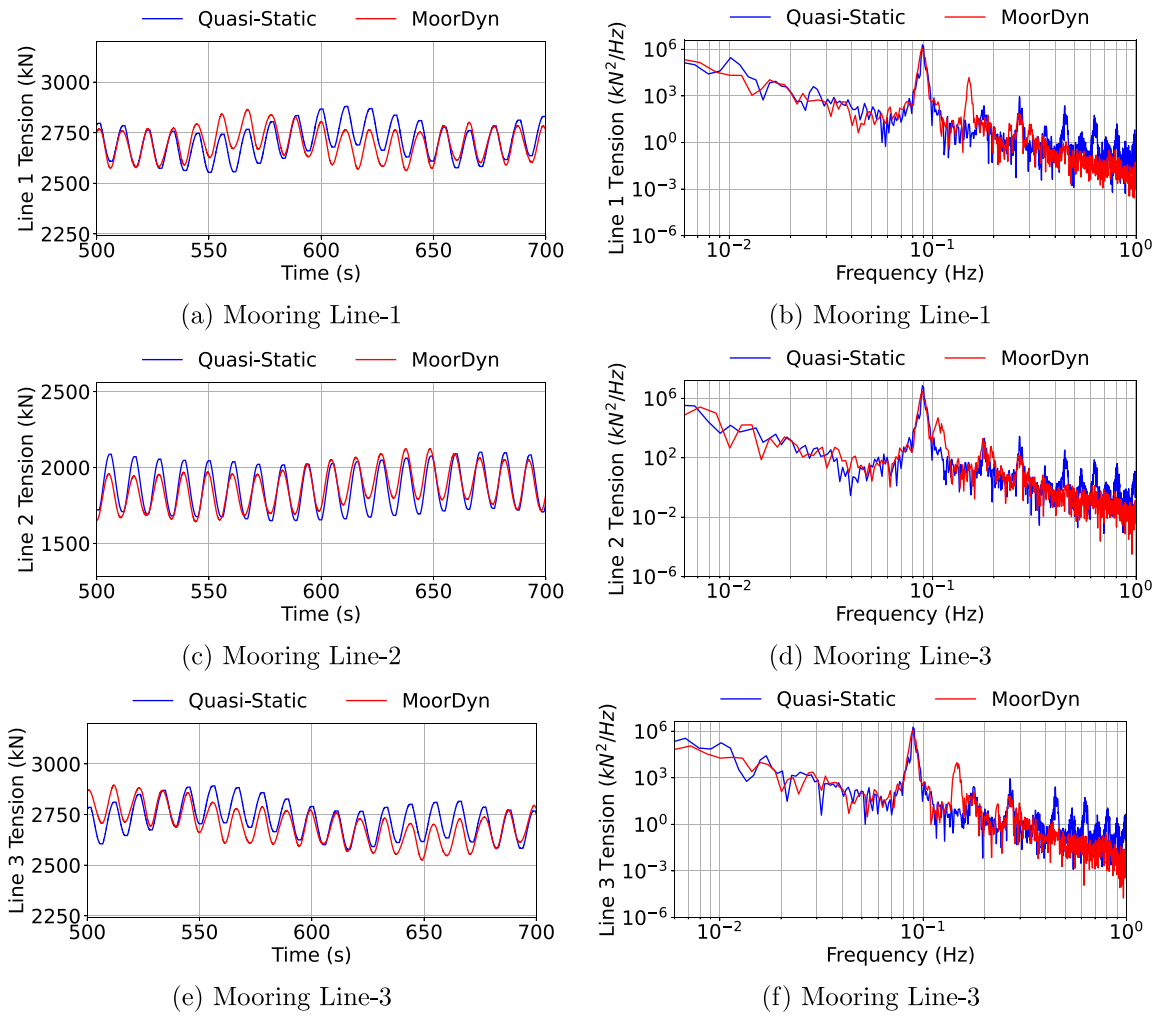

(a) Mooring Line-1 (b) Mooring Line-1

(c) Mooring Line-2 (d) Mooring Line-3

(e) Mooring Line-3 (f) Mooring Line-3

Fig. 19. Comparison of fairlead tensions and corresponding PSDs in Wave-3.

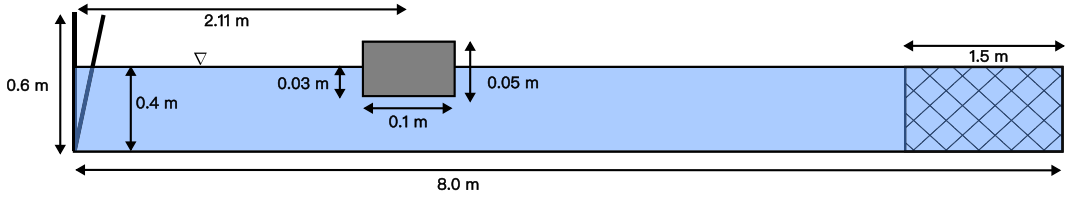

Fig. 20. Schematic of the numerical wave tank.

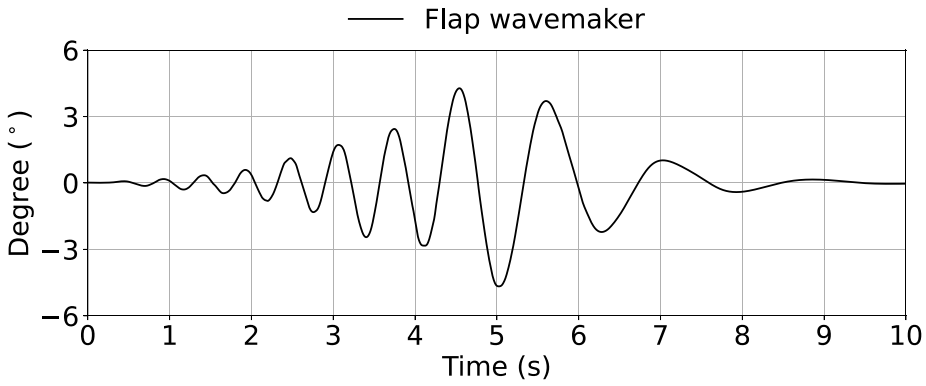

Fig. 21. Time history of the angle of the flap wavemaker.

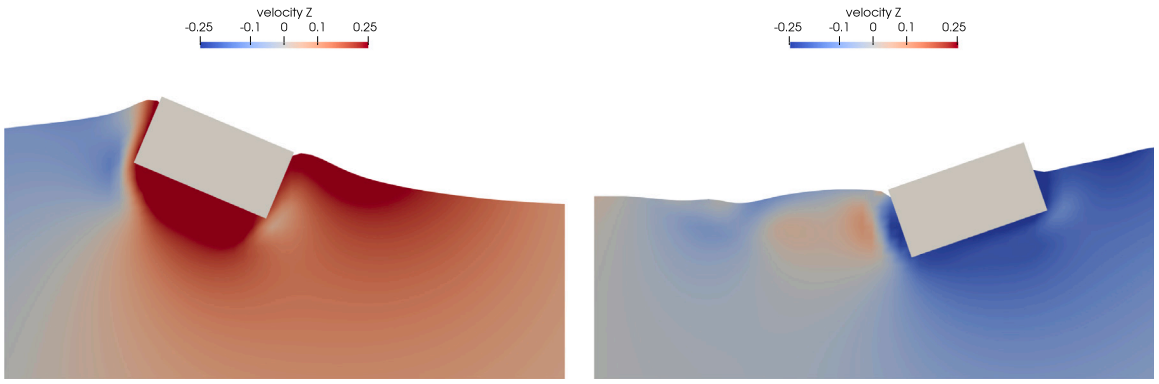

(a) t=7.2 s (b) t=7.59 s

Fig. 22. The motion of the floating box in waves, showing the vertical velocity.

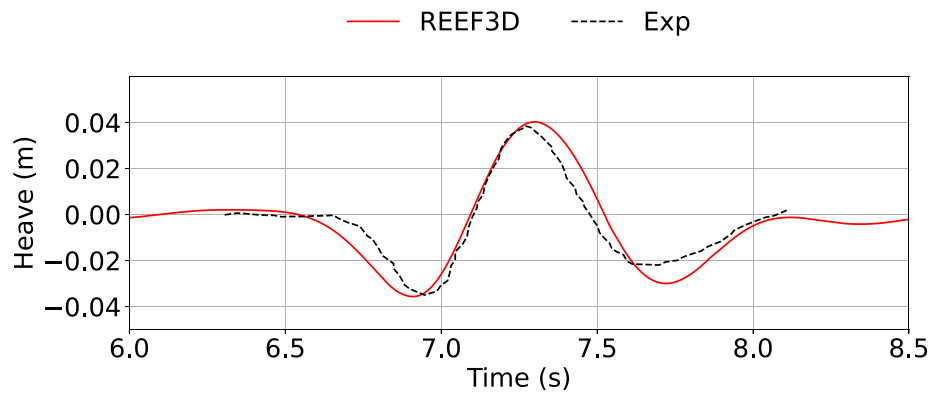

(a) Heave motion over time

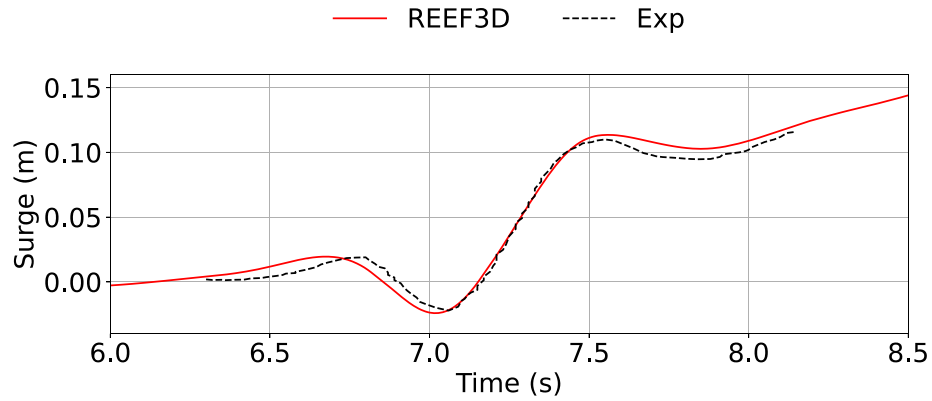

(b) Surge motion over time

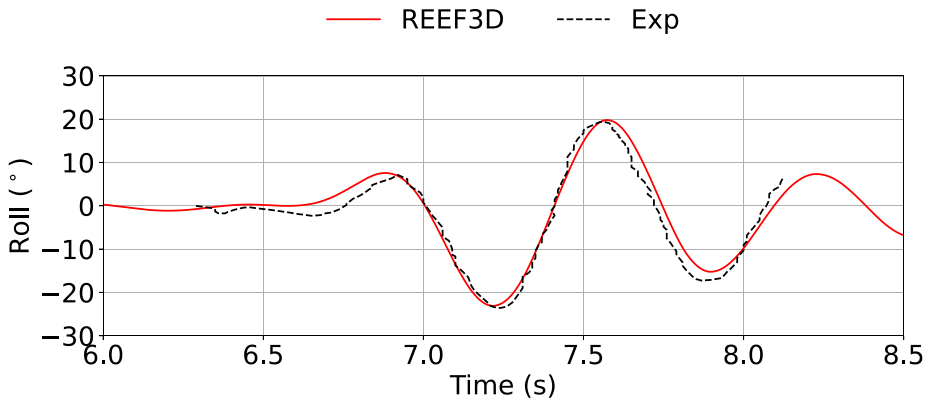

(c) Roll motion over time

Fig. 23. 3DOF motion of the two-dimensional box over time. Comparison of numerical and experimental results.

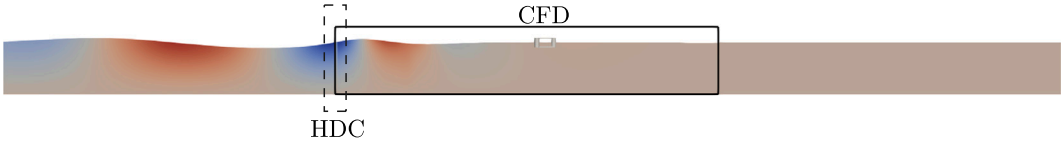

Fig. 24. Schematic of the numerical wave tank, showing CFD-FNPF coupling with HDC.

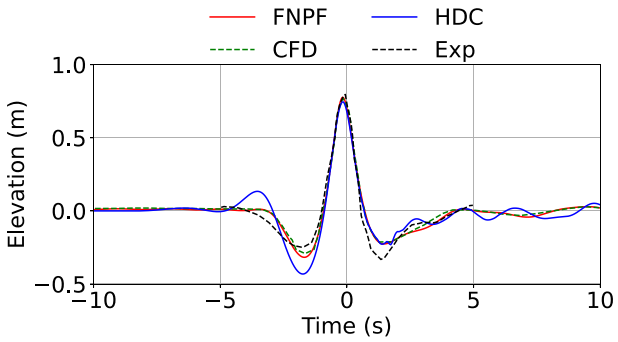

Fig. 25. Comparison of the wave elevation.

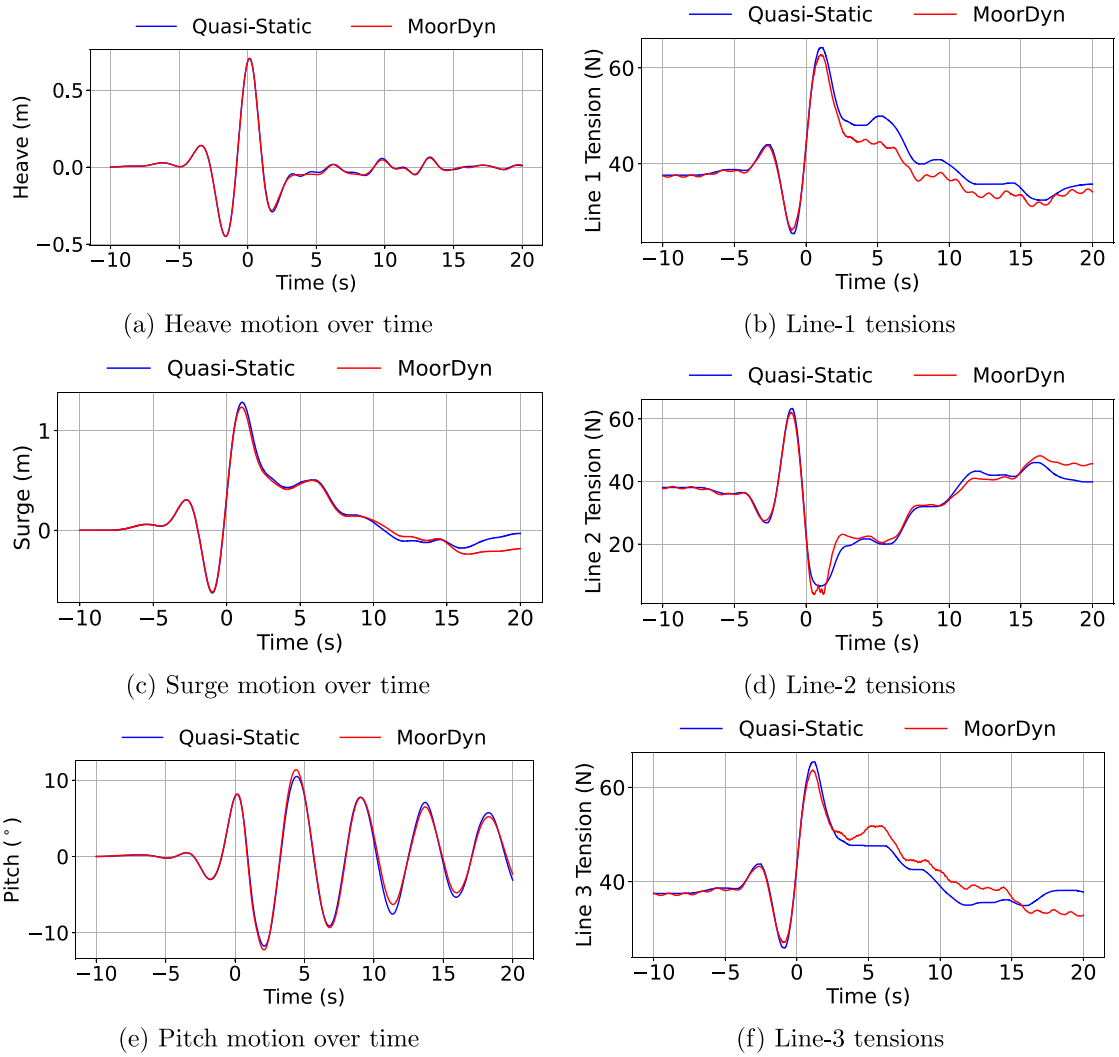

(a) Heave motion over time

(b) Line-1 tensions

(c) Surge motion over time

(d) Line-2 tensions

(e) Pitch motion over time

(f) Line-3 tensions

Fig. 26. Wave excitation motion of the Windmoor FOWT in focused wave and mooring line tensions.

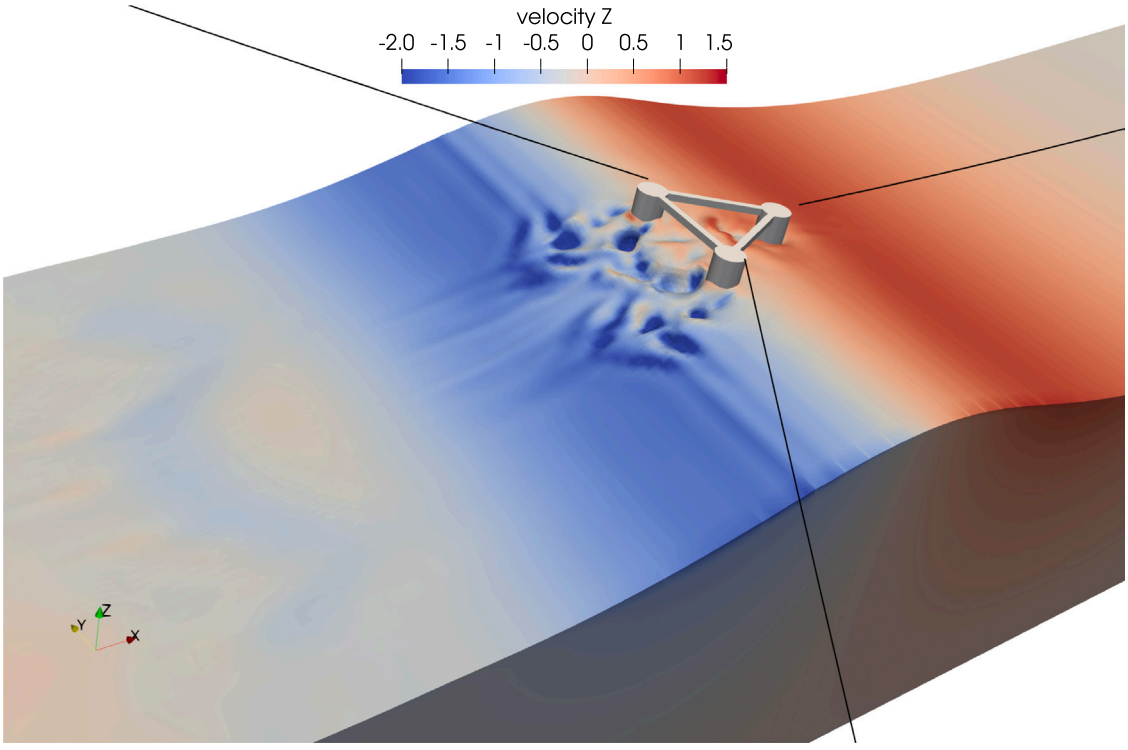

Fig. 27. The FOWT free-surface interaction in the focused waves at focusing time $T_f = 103$ s, showing the vertical velocity contour.

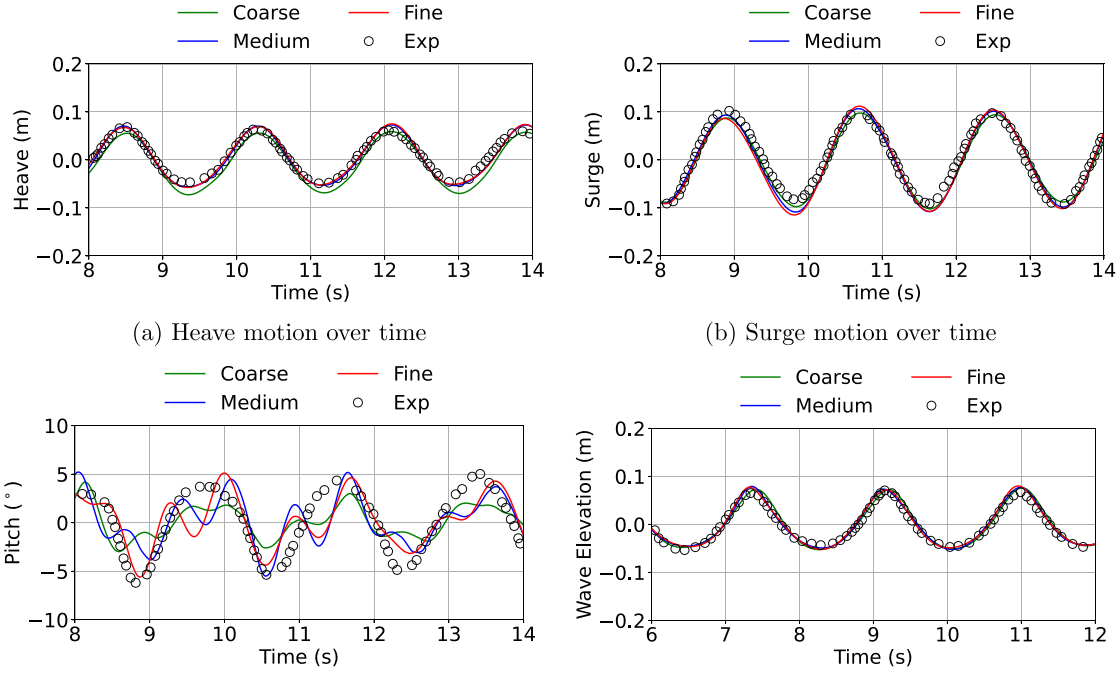

(a) Heave motion over time

(b) Surge motion over time

(c) Pitch motion over time

(d) Wave elevation over time $x = 4.05m$

Fig. A.28. Grid convergence study for the different grid sizes in Wave - 1.

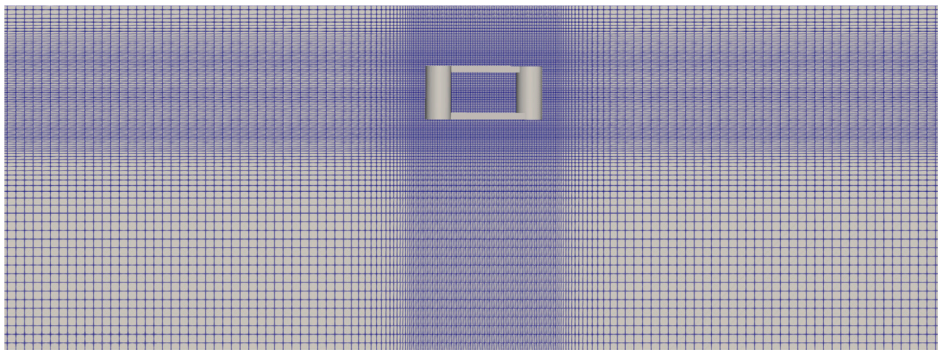

Fig. B.29. Grid stretching around the structure and the free-surface.

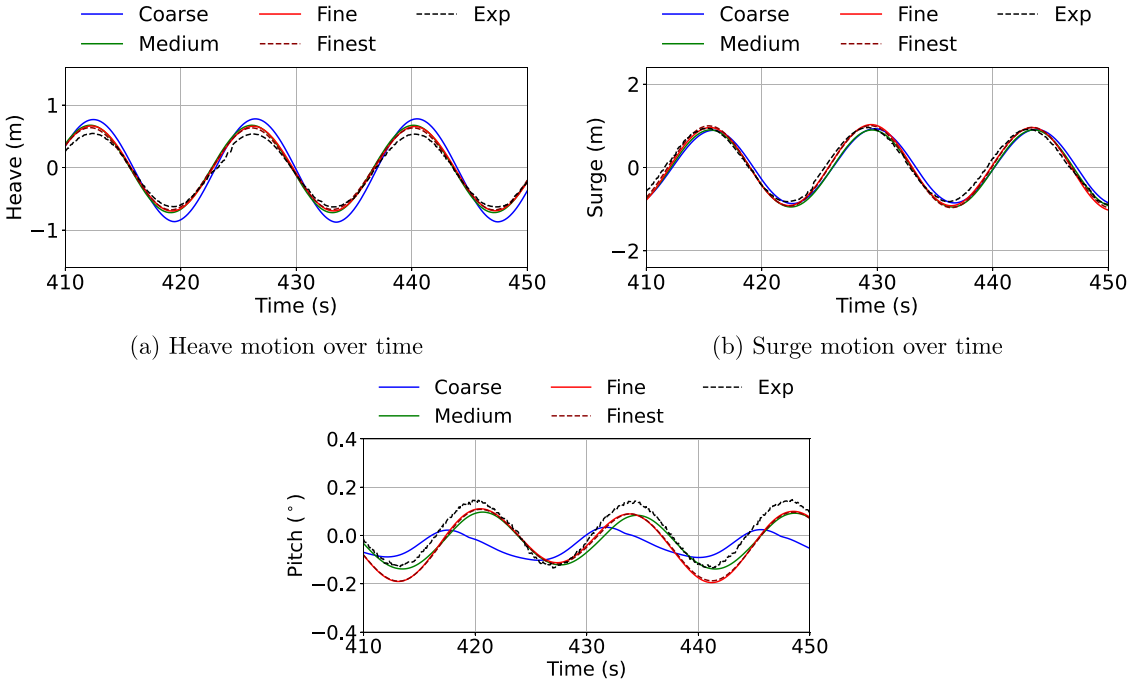

(a) Heave motion over time

(b) Surge motion over time

(c) Pitch motion over time

Fig. B.30. Grid convergence study for the Windmoor FOWT in Wave-1.

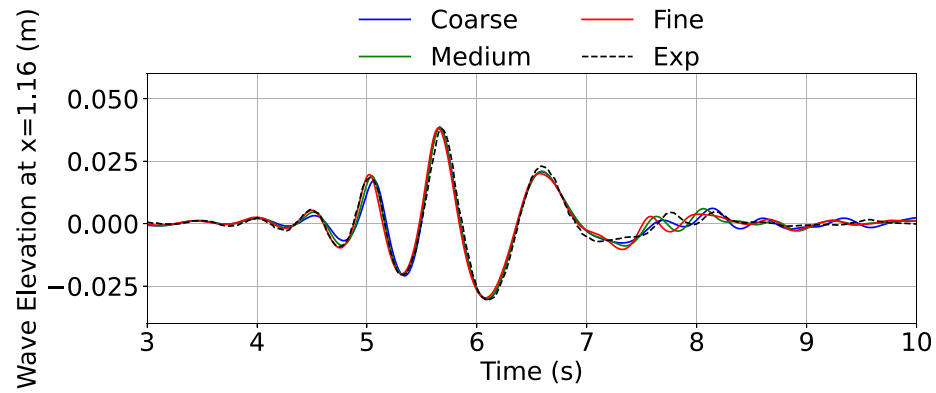

(a) Time history of wave elevation at two probes: x= 1.16 m

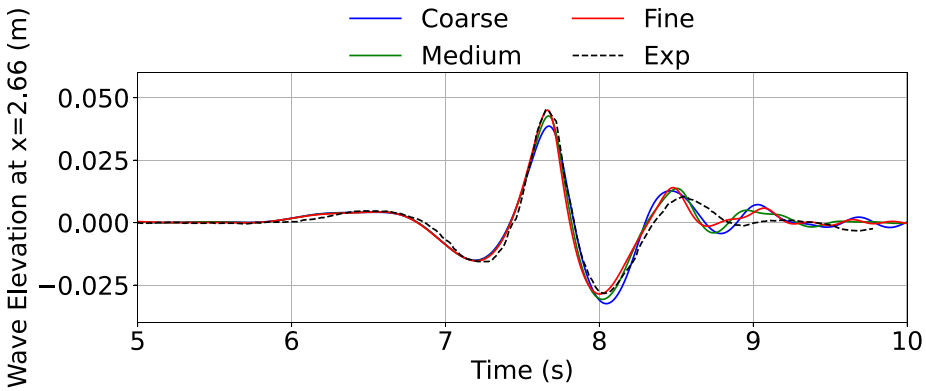

(b) Time history of wave elevation at two probes: x= 2.66 m

Fig. C.31. Time history of the flap wavemaker angle and time series of the experimental and numerical wave elevations.

the experimental results. The result of the coarse grid ($dx = 0.016$) underestimates the peak of the wave at $x = 2.66$, while the results of the medium and fine grids are similar and capture the peak accurately, falling within a range of 1%.

References

Ashby, S., Flagout, R., 1996. A parallel mulitgrid preconditioned conjugate gradient algorithm for groundwater flow simulations. Nucl. Sci. Eng. 124 (1), 145–159.

Barreiro, A., Crespo, A., Dominguez, J., Garcia-Feal, O., Zabala, I., Gomez-Gesteira, M., 2016. Quasi-static mooring solver implemented in SPH. J. Ocean. Eng. Mar. Energy 2, 381–396.

Berthelsen, P.A., Thys, M., Kamath, A.M., Martin, T., Bihs, H.S., 2022. Numerical simulation and comparison with experiments of a floating wind turbine using a direct forcing method. In: Trends in Renewable Energies Offshore Proceedings of the 5th International Conference on Renewable Energies Offshore. Taylor & Francis.

Bihs, H., Kamath, A., Alagan Chella, M., Arntsen, Ø.A., 2019. Extreme wave generation, breaking, and impact simulations using wave packets in REEF3D. J. Offshore Mech. Arct. Eng. 141 (4), 041802.

Bihs, H., Kamath, A., Alagan Chella, M., Pakozdi, C., 2017. Complex geometry handling for a cartesian grid based solver. In: MekIT'17-Ninth National Conference on Computational Mechanics. International Center for Numerical Methods in Engineering (CIMNE).

Bihs, H., Kamath, A., Chella, M.A., Aggarwal, A., Arntsen, Ø.A., 2016. A new level set numerical wave tank with improved density interpolation for complex wave hydrodynamics. Comput. & Fluids 140, 191–208.

Bihs, H., Wang, W., Pakozdi, C., Kamath, A., 2020. Reef3d:: Fnpf—a flexible fully nonlinear potential flow solver. J. Offshore Mech. Arct. Eng. 142 (4).

Bouscasse, B., Colagrossi, A., Marrone, S., Antuono, M., 2013. Nonlinear water wave interaction with floating bodies in SPH. J. Fluids Struct. 42, 112–129.

Burmester, S., Vaz, G., el Moctar, O., 2020. Towards credible CFD simulations for floating offshore wind turbines. Ocean Eng. 209, 107237.

Chen, H., Hall, M., 2022. CFD simulation of floating body motion with mooring dynamics: Coupling MoorDyn with OpenFOAM. Appl. Ocean Res. 124, 103210.

Chen, H., Medina, T.A., Cercos-Pita, J.L., 2024. CFD simulation of multiple moored floating structures using OpenFOAM: An open-access mooring restraints library. Ocean Eng. 303, 117697.

Cheng, P., Huang, Y., Wan, D., 2019. A numerical model for fully coupled aero-hydrodynamic analysis of floating offshore wind turbine. Ocean Eng. 173, 183–196.

Domínguez, J.M., Crespo, A.J., Hall, M., Altomare, C., Wu, M., Stratigaki, V., Troch, P., Cappietti, L., Gómez-Gesteira, M., 2019. SPH simulation of floating structures with moorings. Coast. Eng. 153, 103560.

Gatin, I., Vukčević, V., Jasak, H., 2017. A framework for efficient irregular wave simulations using higher order spectral method coupled with viscous two phase model. J. Ocean. Eng. Sci. 2 (4), 253–267.

Hadžić, I., Hennig, J., Perić, M., Xing-Kaeding, Y., 2005. Computation of flow-induced motion of floating bodies. Appl. Math. Model. 29 (12), 1196–1210.

Hall, M., Buckham, B., Crawford, C., 2014. Evaluating the importance of mooring line model fidelity in floating offshore wind turbine simulations. Wind. Energy 17 (12), 1835–1853.

Hall, M., Buckham, B., Crawford, C., Nicoll, R.S., 2011. The importance of mooring line model fidelity in floating wind turbine simulations. In: OCEANS'11 MTS/IEEE KONA. IEEE, pp. 1–8.

Hall, M., Goupee, A., 2015. Validation of a lumped-mass mooring line model with DeepCwind semisubmersible model test data. Ocean Eng. 104, 590–603.

Huang, H., Chen, H.-C., 2020. Investigation of mooring damping effects on vortex-induced motion of a deep draft semi-submersible by coupled CFD-FEM analysis. Ocean Eng. 210, 107418.

Jacobsen, N.G., Fuhrman, D.R., Fredsøe, J., 2012. A wave generation toolbox for the open-source CFD library: OpenFoam®. Internat. J. Numer. Methods Fluids 70 (9), 1073–1088.

Jeon, W., Park, S., Cho, S., 2023. Moored motion prediction of a semi-submersible offshore platform in waves using an OpenFOAM and MoorDyn coupled solver. Int. J. Nav. Archit. Ocean. Eng. 15, 100544.

Jiang, G., Peng, D., 2000. Weighted ENO schemes for Hamilton Jacobi equations. SIAM J. Sci. Comput. 21, 2126–2143.

Jiang, G.-S., Shu, C.-W., 1996. Efficient implementation of weighted ENO schemes. J. Comput. Phys. 126 (1), 202–228.

Kamath, A., Martin, T., Wang, W., Pakozdi, C., Bihs, H., 2022. Identification and investigation of extreme events on marine structures using ALE approach and hydrodynamic coupling of Navier Stokes-and Laplace equation-based models. In:

International Conference on Offshore Mechanics and Arctic Engineering. Vol. 85895, American Society of Mechanical Engineers, V05AT06A038.
Kim, S.-H., Yamashiro, M., Yoshida, A., 2010. A simple two-way coupling method of BEM and VOF model for random wave calculations. Coast. Eng. 57 (11–12), 1018–1028.
Larkermani, E., Bihs, H., Winckelmans, G., Müller, B., Georges, L., 2025. High-fidelity explicit large eddy simulations of airflows inside buildings using the immersed boundary method and orthogonal grids. Phys. Fluids 37 (3), 035174. http://dx.doi.org/10.1063/5.0258912.
Li, P., Cheng, P., Wan, D., Xiao, Q., 2015. Numerical simulations of wake flows of floating offshore wind turbines by unsteady actuator line model. In: Proceedings of the 9th International Workshop on Ship and Marine Hydrodynamics, Glasgow, UK. pp. 26–28.
Liu, Y., Xiao, Q., Incecik, A., Peyrard, C., Wan, D., 2017. Establishing a fully coupled CFD analysis tool for floating offshore wind turbines. Renew. Energy 112, 280–301.
Lozon, E., Hall, M., 2023. Coupled loads analysis of a novel shared-mooring floating wind farm. Appl. Energy 332, 120513.
Martin, T., A., T., Bihs, H., 2021a. Numerical framework for modelling the dynamics of open ocean aquaculture structures in viscous fluids. Appl. Ocean Res. 106, 102410.
Martin, T., Kamath, A., Bihs, H., 2021b. Accurate modeling of the interaction of constrained floating structures and complex free surfaces using a new quasistatic mooring model. Internat. J. Numer. Methods Fluids 93 (2), 504–526.
Masciola, M., Jonkman, J., Robertson, A., 2013a. Implementation of a multisegmented, quasi-static cable model. In: ISOPE International Ocean and Polar Engineering Conference. ISOPE, pp. ISOPE–I.
Masciola, M., Robertson, A., Jonkman, J., Coulling, A., Goupee, A., 2013b. Assessment of the importance of mooring dynamics on the global response of the DeepCwind floating semisubmersible offshore wind turbine. In: ISOPE International Ocean and Polar Engineering Conference. ISOPE, pp. ISOPE–I.
Masciola, M., Robertson, A., Jonkman, J., Driscoll, F., 2011. Investigation of a FAST-OrcaFlex Coupling Module for Integrating Turbine and Mooring Dynamics of Offshore Floating Wind Turbines. Tech. Rep., National Renewable Energy Lab.(NREL), Golden, CO (United States).
Miquel, A.M., Kamath, A., Alagan Chella, M., Archetti, R., Bihs, H., 2018. Analysis of different methods for wave generation and absorption in a CFD-based numerical wave tank. J. Mar. Sci. Eng. 6 (2), 73.
Osher, S., Sethian, J.A., 1988. Fronts propagating with Curvature-Dependent speed: Algorithms based on Hamilton-Jacobi formulations. J. Comput. Phys. 79, 12–49.
Palm, J., Eskilsson, C., Bergdahl, L., 2017. An hp-adaptive discontinuous Galerkin method for modelling snap loads in mooring cables. Ocean Eng. 144, 266–276.
Palm, J., Eskilsson, C., Paredes, G.M., Bergdahl, L., 2016. Coupled mooring analysis for floating wave energy converters using CFD: Formulation and validation. Int. J. Mar. Energy 16, 83–99.
Peng, D., Merriman, B., Osher, S., Zhao, H., Kang, M., 1999. A PDE-based fast local level set method. J. Comput. Phys. 155, 410–438.
Robaux, F., Benoit, M., 2022. Assessment of one-way coupling methods from a potential to a viscous flow solver based on domain-and functional-decomposition for fixed submerged bodies in nonlinear waves. Eur. J. Mech. B Fluids 95, 315–334.
Shu, C., Osher, S., 1988. Efficient implementation of essentially non-oscillatory shock-capturing schemes. J. Comput. Phys. 77 (2), 439–471.
Silva de Souza, C.E., Berthelsen, P.A., Eliassen, L., Bachynski, E.E., Engebretsen, E., Haslum, H., 2021. Definition of the INO WINDMOOR 12 MW base case floating wind turbine.
Soydan, A., Wang, W.W., Bihs, H., 2025. An improved direct forcing immersed boundary method for floating body simulations in waves. Appl. Ocean Res. (ISSN: 0141-1187) 158, 104523. http://dx.doi.org/10.1016/j.apor.2025.104523.
Spalart, P.R., Moser, R.D., Rogers, M.M., 1991. Spectral methods for the Navier-Stokes equations with one infinite and two periodic directions. J. Comput. Phys. 96 (2), 297–324.
Sussman, M., Smereka, P., Osher, S., 1994. A level set approach for computing solutions to incompressible Two-Phase Flow. J. Comput. Phys. 114, 146–159.
Thys, M., Souza, C., Sauder, T., Fonseca, N., Berthelsen, P.A., Engebretsen, E., Haslum, H., 2021. Experimental investigation of the coupling between aero-and hydrodynamical loads on a 12 mw semi-submersible floating wind turbine. In: International Conference on Offshore Mechanics and Arctic Engineering. Vol. 85192, American Society of Mechanical Engineers, V009T09A030.
Timmermans, L.J., Minev, P.D., Van De Vosse, F.N., 1996. An approximate projection scheme for incompressible flow using spectral elements. Internat. J. Numer. Methods Fluids 22 (7), 673–688.
Tran, T.T., Kim, D.-H., 2016. Fully coupled aero-hydrodynamic analysis of a semi-submersible FOWT using a dynamic fluid body interaction approach. Renew. Energy 92, 244–261.
Tran, T.T., Kim, D.-H., 2018. A CFD study of coupled aerodynamic-hydrodynamic loads on a semisubmersible floating offshore wind turbine. Wind. Energy 21 (1), 70–85.
Vaz, G., Jaouen, F., Hoekstra, M., 2009. Free-surface viscous flow computations: Validation of URANS code FRESCO. In: International Conference on Offshore Mechanics and Arctic Engineering. 43451, pp. 425–437.
van der Vorst, H., 1992. BiCGStab: A fast and smoothly converging variant of Bi-CG for the solution of nonsymmetric linear systems. SIAM J. Sci. Comput. 13, 631–644.
Wang, Y., Chen, H.-C., Koop, A., Vaz, G., 2021. Verification and validation of CFD simulations for semi-submersible floating offshore wind turbine under pitch free-decay motion. Ocean Eng. 242, 109993.
Wang, Y., Chen, H.-C., Koop, A., Vaz, G., 2022a. Hydrodynamic response of a FOWT semi-submersible under regular waves using CFD: Verification and validation. Ocean Eng. 258, 111742.
Wang, L.-z., Guo, Z., Yuan, F., 2010. Quasi-static three-dimensional analysis of suction anchor mooring system. Ocean Eng. 37 (13), 1127–1138.
Wang, W., Pákozdi, C., Kamath, A., Martin, T., Bihs, H., 2022b. Hydrodynamic coupling of viscous and nonviscous numerical wave solutions within the open-source hydrodynamics framework reef3d. J. Offshore Mech. Arct. Eng. 144 (4), 041903.
Wei, Y., Yu, S., Jin, P., Huang, L., Elsherbiny, K., Tezdogan, T., 2024. Coupled analysis between catenary mooring and VLFS with structural hydroelasticity in waves. Mar. Struct. 93, 103516.
Wu, M., Stratigaki, V., Troch, P., Altomare, C., Verbrugghe, T., Crespo, A., Cappietti, L., Hall, M., Gómez-Gesteira, M., 2019. Experimental study of a moored floating oscillating water column wave-energy converter and of a moored cubic box. Energies 12 (10), 1834.
Xu, H., Zhang, Y., Santo, H., Chua, K.H., Law, Y.Z., Chan, E.S., 2021. Coupling of potential flow and CFD model for fluid and structure interactions. In: International Conference on Offshore Mechanics and Arctic Engineering. Vol. 85185, American Society of Mechanical Engineers, V008T08A009.
Yu, S., Ransley, E., Qian, L., Zhou, Y., Brown, S., Greaves, D., Hann, M., Holcombe, A., Edwards, E., Tosdevin, T., Jagdale, S., Li, Q., Zhang, Y., Zhang, N., Yan, S., Ma, Q., Tagliafierro, B., Capasso, S., Martínez-Estévez, I., Göteman, M., Bernhoff, H., Karimirad, M., Domínguez, J.M., Altomare, C., Viccione, G., Crespo, A.J., Gómez-Gesteira, M., Eskilsson, C., Fernandez, G.V., Andersen, J., Palm, J., Niosi, F., Dell'Edera, O., Sirigu, M., Ghigo, A., Bracco, G., Cui, F., Chen, S., Wang, W., Zhuo, Y., Li, Y., Peyrard, C., Benguigui, W., Barcet, M., Robaux, F., Benoit, M., Teles, M., Ntouras, D., Manolas, D., Papadakis, G., Riziotis, V., Zheng, Z., Lei, W., Wang, R., Chen, J., Shao, Y., Visbech, J., Bingham, H.B., Engsig-Karup, A.P., Zhou, Y., Cai, Y., Zhao, H., Shi, W., Li, X., Zeng, X., Xue, Y., Zhuang, T., Wan, D., Engel, G., Tierno, M., Ducrozet, G., Bouscasse, B., Leroy, V., Ferrant, P., Barajas, G., Lara, J.L., 2025. Modelling the hydrodynamic response of a floating offshore wind turbine – a comparative study. Appl. Ocean Res. (ISSN: 0141-1187) 155, 104441. http://dx.doi.org/10.1016/j.apor.2025.104441.
Zhang, Y., Xu, H., Law, Y., Santo, H., Magee, A., 2023. Hydrodynamic analysis and validation of the floating DeepCwind semi-submersible under 3-h irregular wave with the HOS and CFD coupling method. Ocean Eng. 287, 115701.
Zhong, W., Zhao, W., Wan, D., Zhao, Y., 2024. Comparison study on mooring line models for hydrodynamic performances of floating offshore wind turbines. Ocean Eng. 296, 117083.
Zhou, Y., Xiao, Q., Liu, Y., Incecik, A., Peyrard, C., Li, S., Pan, G., 2019. Numerical modelling of dynamic responses of a floating offshore wind turbine subject to focused waves. Energies 12 (18), 3482.